Bimetallic Nanoparticles for Sustainable Electrocatalysis

John Tyler Brosnahan
Haymarket, Virginia

B.S., College of William & Mary, 2015

A Thesis presented to the Graduate Faculty
of the University of Virginia in Candidacy for the Degree of
Master of Science

Department of Chemistry

University of Virginia
May 2021

Abstract

There is now a large body of scientific evidence suggesting that human carbon emissions and carbon waste are causing changes to the earth's atmosphere and ecosystems. Many societies agree that we should broadly deploy new technologies to try to minimize the negative impacts of rapid technological advancement during the last two centuries. Heterogenous electrocatalysis will play an important role in a future, more sustainable chemistry landscape, with potential to make contributions to renewable solutions such as CO2 valorization, green hydrogen, biomass utilization, energy, and transportation. Electrocatalysis can often facilitate the same conversions as in commercial industrial chemistry, but with more benign conditions, less waste, and electricity as the energy input, which can be generated by existing renewable methods including solar, wind, and fuel cells. Nanodimensional metal particles are active electrocatalysts, but for experimental conclusions to be reliable and for making detailed conclusions about surface effects in nanoparticle catalysis, repeatable synthetic procedures for are necessary. Solution-phase nanoparticle synthesis is an adaptable technique for obtaining morphologically homogenous nanocrystals in the lab, where nucleation and micellar growth are controlled to obtain consistent samples. This research utilizes a solution-phase procedure for monodisperse AgPd alloy nanoparticles with tunable alloy composition, which are tested as electrocatalysts in the reductive hydrogenation of furfural to reveal relationships between alloy composition and electrocatalytic efficiency towards furfuryl alcohol production.

Publications

Brosnahan, J. T., Zhang, Z., Yin, Z., Zhang, S., Electrocatalytic Reduction of Furfural with High Selectivity to Furfuryl Alcohol Using AgPd Alloy Nanoparticles, *Nanoscale*, **2021**, d0nr07676g.

Zhang, Z., Liu, C., Brosnahan, J. T., Zhou, H., Xu, W., Zhang, S., Revealing Structure Evolution of PbS Nanocrystal Catalysts in the Electrochemical CO2 Reduction Using in situ Synchrotron Radiation X-ray Diffraction, *Journal of Materials Chemistry A*, **2019**, *7*, 23775-23780.

Peng, Y., Cui, M., Zhang, Z., Shu, S., Shi, X., Brosnahan, J. T., Liu, C., Zhang, Y., Godbold, P., Zhang, X., Dong, F., Jiang, G., Zhang, S., Bimetallic Composition-Promoted Electrocatalytic Hydrodechlorination Reaction on Silver-Palladium Alloy Nanoparticles, *ACS Catalysis*, **2019**, *9*, 10803-10811.

Wang, Z., Huang, Z., Brosnahan, J. T., Zhang, S., Guo, Yanglong, Guo, Yun, Wang, L., Wang, Y., Zhan, W., Ru/CeO2 Catalyst with Optimized CeO2 Support Morphology and Surface Facet for Propane Combustion, *Environmental Science and Technology*, **2019**, *53*, 5349-5358.

Dedication

This work is dedicated to my mother, father, sister, and grandparents, who have always given me love and support in what I do. Thanks also go out to my advisor, Sen Zhang, and my labmates in his research group who have been good friends and learning partners.

Table of Contents

List of Figures and Tables

Chapter 1

Solution-Phase Colloidal Synthesis of Metal, Metal-Oxide, and Alloy Nanoparticles

1.1 A Brief Introduction to Nanomaterials

The prefix “nano” appears frequently today in scientific and popular culture, largely due to a recent boom in technological interest for developing nanoscale materials. The term nanomaterial applies broadly to a crystalline or amorphous solid whose size is confined to the 1-100 nanometer regime in at least one dimension.[1] Devices like cell phones, televisions and computers have decreased in overall size since their inception, and interest in the nanoscale has revealed that materials with boundaries confined to such small regions, nearly the atomic level (10 Angstrom = 1 nm), display different physical and electronic properties than the bulk and microscale counterparts.[2]

Carbon materials are studied at the nanoscale in part due to the conductivity characteristics well known to solid phases of this abundant element. Graphene is one example of a two-dimensional nanomaterial, an isolated sheet of graphitic carbon atoms arranged in a planar hexagonal lattice, whereas graphite consists of stacked graphene layers.[3] Each atom in a sheet of graphene contributes three valence electrons to sigma bonding with its neighbors, and a fourth to a quasi-conduction band that encompasses the single layer material in which electrons are highly mobile.[4] Graphene conducts heat and electricity effectively along its plane, and it boasts one of the highest tensile strengths ever measured.[5] If a sheet of graphene is rolled into a tube shape, it becomes a one-dimensional nanomaterial called a carbon nanotube, confined to the nano regime in two dimensions. Carbon nanotubes also have good conductivity along their length, with more morphological stability than graphene during fabrication processes. Lastly, carbon materials like carbon dots, fullerenes, and nanodiamonds are zero-dimensional, with all three physical dimensions limited to the nanometer scale.

Metals and metal oxides exhibit unique electronic behaviors when structured at the nanoscale. Quantum dots (QDs), typically small metal chalcogenide nanospheres, are another class of nanomaterial which have made their way into household devices due to their unique optoelectronic properties.[6] Their functionality is derived from a phenomenon of the electronic structure in semiconductor nanocrystals, which can be observed in discrete energetic levels when the diameter of the nanoparticles is on the same scale as the wavelength of an excited electron in the material. An exciton, or electron-hole pair, is formed when a semiconductor absorbs a photon with higher energy than its band gap, and the Bohr radius of that exciton is confined to a small space in a QD.[7] An exciton in a QD experiences a more discrete electronic environment than the exciton in a bulk crystal which would behave as a free carrier with a wide range until recombination of the electron and hole constituents, an event which would release a photon with energy corresponding to the bulk material's band gap. The energy of optical emission from electron-hole recombination can be defined through nanoscale size control in QDs, such that when illuminated with UV light, QDs with different size can emit photons of different visible color due to this quantum confinement of the excited electronic state. Size and shape selectivity during synthesis of QDs enables tunable emissions across a wide spectrum, so QDs are utilized in next-generation LED displays, solar cells, sensors, transistors, and more.[8-11]

Metallic nanoparticles also possess special physical and optical properties absent from the bulk phase, and one area of their applicability is heterogenous catalysis.[12] Catalytic reactions require an active site where a substrate interacts with the catalyst. If the catalyst is a metal surface, nanoscale metal particles provide much higher atom utilization efficiency compared with a bulk metal, since they leave significantly fewer metal atoms inaccessible to reactants in the interior of the crystal lattice. Nanoparticles form more catalytic adsorbates per atom of metal present, allowing for more reactions to occur at a given time than if the same amount of metal were structured as one bulk crystal. Furthermore, the electrons at a nanoparticle surface tend to have higher energy than those on a bulk surface. The atoms on any metal surface are undercoordinated relative to more stable atoms in the interior of the crystal, and the exterior orbitals at a metal surface are comparatively more reactive. A bulk catalyst is considered to have a mostly flat active surface, but in a nanocrystal, there are edges and corners in three dimensions where the metal atoms and their orbitals are more exposed to the reaction medium. This effect can be used to explain why some bulk metals do not exhibit catalytic reactivity, but nanoparticles composed of the same metal might be active, with gold being one example.[13]

1.2 Colloidal Synthesis of Metal Based Nanoparticles

Metal nanoparticles can be obtained by a variety of methods generally categorized as either "top-down" or "bottom-up" approaches. A top-down technique is a physical one, where a bulk metal is broken down into nano-sized pieces. These are often energy-intensive processes that lack nuanced control over crystallite size and surface structuring.[14] Consequently, top-down approaches are mostly unfavorable for applications where consistency of nanoparticle size and shape is vital, including some academic studies of nanoparticle catalysis. Bottom-up methods, on the other hand, take a chemical route to nanoparticle development; an atomic metal precursor is distributed in some medium where crystal nucleation and growth can occur, sometimes coinciding with the introduction of some heat as activation energy. Multiple methods for the development of nanoparticles can be classified as bottom-up, most of which are less expensive and more efficient than physical processes. This work focuses on colloidal synthesis of nanoparticles, another wet chemical recipe which has the benefit of not requiring a support material on which nanoparticles grow. Instead, nanoparticles nucleate independently in solution and grow isometrically as individual units. Colloidal nucleation and growth enables the production of freely suspended samples in which all particles have the same size and shape. A nanoparticle suspension can then be fabricated into a range of materials. The versatility of solution-phase colloidal nanoparticle synthesis sets it apart from the other known approaches to producing monodisperse metal nanocrystals.

Colloidal synthesis of metal nanoparticles from organic solution is summarized by nucleation of metallic or metal oxide clusters, followed by ligand-assisted growth as separated micellar bodies. One benefit of the liquid approach is each of its steps can be controlled in the fume hood using a simple glassware apparatus and relatively low temperatures. In a typical synthesis, only metal salt precursors (metal acetate, acetylacetonate, chloride) and high boiling point organic solvents (e.g., 1-octadecene, benzyl ether) are consumed in a one-pot reaction. As a particle grows in solution, a polar hydrocarbon (e.g., oleylamine, oleic acid) species binds to the energetic outer-layer atoms through a terminal functional group, effectively passivating the solid surface, while the nonpolar remainder of the molecule extends away from the center of the nanocrystal. This collective layer of bound surfactant species forms a micelle which isolates each nanoparticle. During nanoparticle growth, surfactant molecules occupy the same surface sites at which metal atoms want to add, and the binding strength of a given ligand will vary across different surface facets of the same material. The rate of precursor addition can be quite different at different facets due to energetic barriers to inserting an atom beneath the ligand layer, so much so that in some scenarios, nanoparticles might only grow one-dimensionally, from one facet. Selection of the surfactant species can be utilized for kinetic control to obtain differently shaped and sized nanocrystals with the same composition.

1.2.1 La Mer Theory of Colloidal Particle Nucleation

For the most part, a general theory attributed to La Mer can be used to summarize the concepts of colloidal nanoparticle synthesis.[15] Figure 1.1 shows a plot representing the theory. A metal nanocrystal nucleation event occurs in colloidal solution when some dissolved metal precursor species spikes in concentration to the point of supersaturation, displayed as the dotted line separating period I from period II. Supersaturation is then relaxed by the formation of atomic clusters, and the concentration of dissolved precursor drops as elevated reaction temperatures

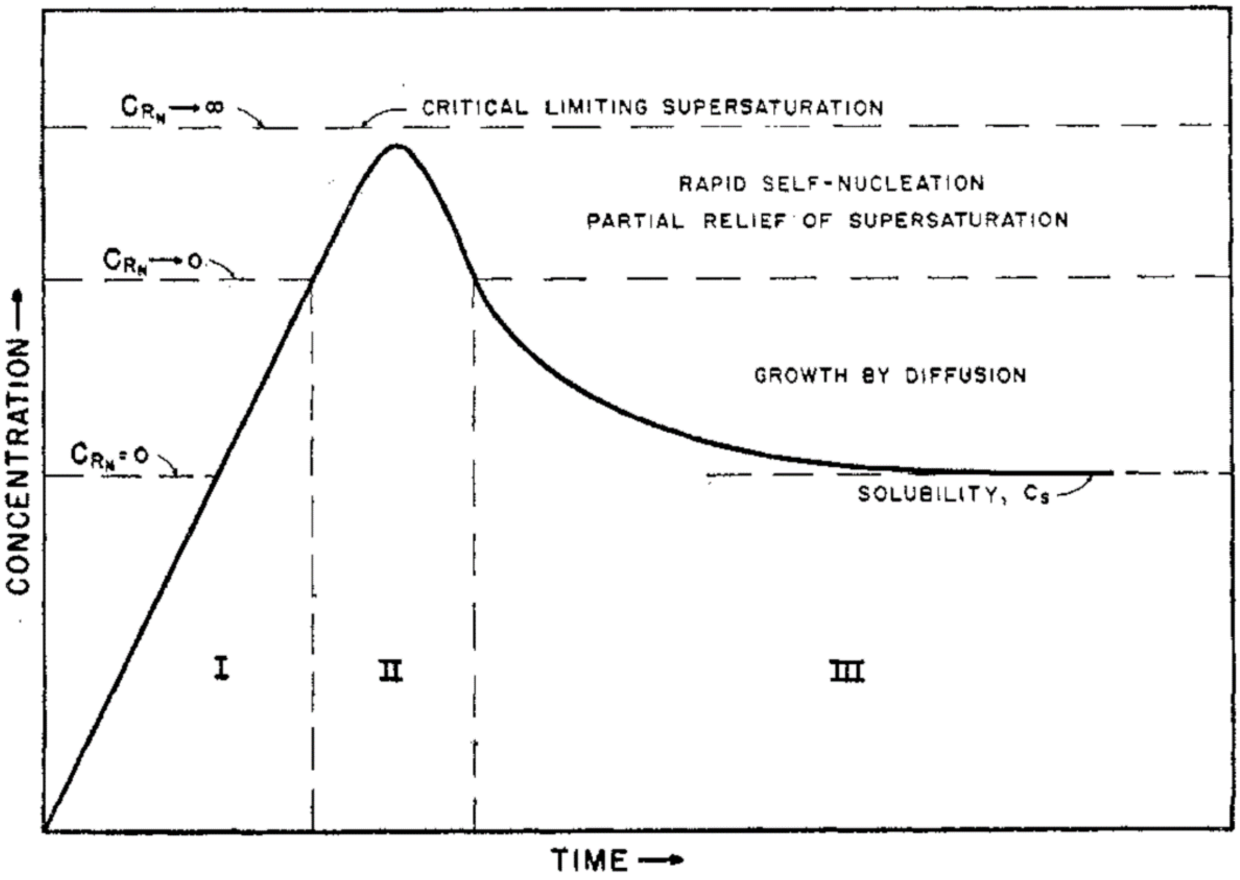

Figure 1.1. Schematic representation of colloidal particle nucleation with the concentration of nucleating species plotted against time. Adopted from La Mer, 1952.[15]

drive rapid growth of nanoparticles with solvated metal precursors adding on to the existing crystalline nuclei (period III). Ostwald ripening of particles refers to the process by which grown particles will undergo a spontaneous size-selection event, where small particles with higher surface energy will re-dissolve into atomic monomers and grow onto a larger particle’s surface. This process is held out anywhere from mere seconds to many hours during synthesis to allow the precursor concentration to approach some equilibrium level of dissolution. By controlling the rate and duration of each of these steps, monodisperse metal nanoparticles of countless compositions, shapes, and sizes can be developed and optimized.

Optimal reaction parameters for a given nanoparticle synthesis can be pursued experimentally to grow homogenous nanoparticles with the same size and crystalline facets. The species of solvent, surfactant, and metal precursor contribute to nanoparticle formation and growth dynamics, as do the temperature, moisture, oxygen, and other factors. Chemical reductants might be introduced to incite rapid metallic precursor formation, such that a small, limited window of size selection precedes nucleation of particles, with the goal of obtaining a monodisperse product. A similar approach to quick nucleation is to inject metal precursor directly into a hot organic solution, causing rapid decomposition of the metal precursor.

1.2.2 Experimental Setup

The synthesis methods described in this work all use the wet chemical technique introduced in this chapter. Refer to figure 1.2 for a visual representation of the typical reaction setup. A four-neck glass flask containing the reaction solution is clamped in place above a stirring plate and fitted with a heating mantle. The heating mantle is connected to a digital heating controller and coupled to a temperature probe fixed in the reaction solution. A Schlenk line is connected to the flask so that vacuum and inert gas conditions can be toggled to remove air and moisture from the

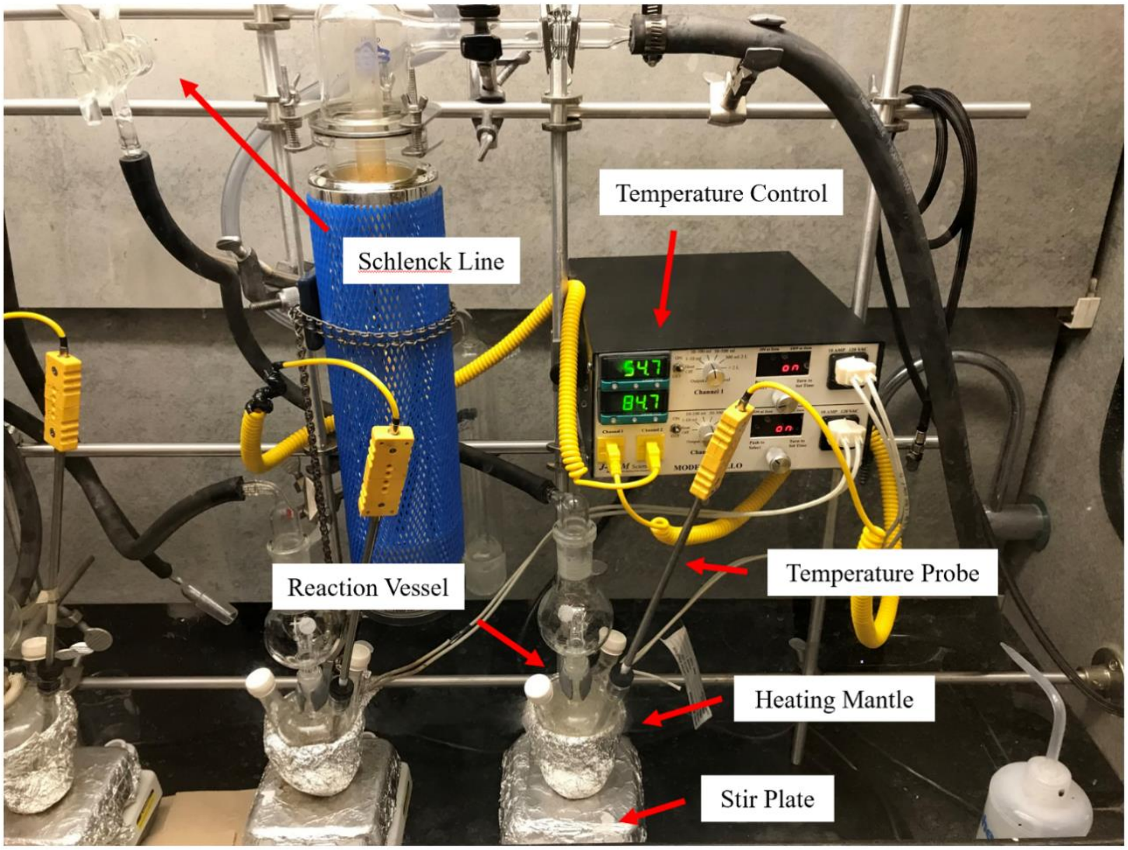

Figure 1.2. Typical fume hood reaction setup for all wet chemical synthesis described in this work.

reaction system. Air- and moisture-sensitive reactants are stored in the N_2 environment of the glovebox and can be transferred into the closed reaction system, if needed. A large assortment of metal salt precursors and organic liquids can be reacted inside this simple setup, giving the researcher the potential to produce a vast array of samples, making modulations from one synthesis to the next.

After synthesizing metal nanoparticles from solution, they can be collected by a precipitation and centrifugation process. The hydrophobic chains of the surface ligands covering each nanoparticle allow their dissolution in nonpolar solvents, like the ones in the reaction solution.

Adding a polar alcohol like 2-propanol or ethanol will cause precipitation of the metal nanocrystals from the quenched reaction solution, and the particles can be separated by centrifugation. The nanocrystals are then re-dissolved in a nonpolar solvent like hexane for storage and later use. Further nanoparticle processing for electrocatalytic applications is discussed later.

One noteworthy advantage of the wet chemical approach for nanoparticle synthesis is its versatility. Solution-phase reactions to produce nanoparticles are often completed within a few hours, and each chemical in the synthesis can be exchanged with a similar candidate for comparative study. Temperatures and injections are manually controlled and an environment without oxygen or moisture can be handled accessibly in the fume hood, saving the additional steps required during synthetic operation in a glovebox. Furthermore, the library of accessible metal nanoparticles from one general synthetic technique is expansive. Numerous metals are compatible with the same solvents and surfactants, and the general nucleation theory discussed previously can be applied across the periodic table. As a graduate student in the Zhang lab, I have synthesized well over 50 different types of metallic and metal oxide nanoparticles using the same basic experimental setup.

1.2.3 Characterization of Nanocrystals

Transmission Electron Microscopy (TEM)

TEM images allow for the observation of nanoparticle shape and size. Transmission electron microscopy (TEM) images were obtained at UVA on a Tecnai Spirit at 120 kV equipped with a tungsten filament. For sampling, nanoparticles were diluted in hexane and one drop was carefully dispensed over the flat surface of copper grid coated with Formvar carbon.

High Resolution Transmission Electron Microscopy

High resolution TEM imaging provides visual evidence of atomic lattice arrangements and crystalline surface facets. The HRTEM images were generated using a JEOL 2100F (200 kV) with a field-emission electron source. Samples are prepared in the same manner as for TEM (section 1.4.1).

Scanning TEM – Electron Energy Loss Spectroscopy (STEM-EELS)

STEM-EELS is used to determine the physical location of different elements throughout a single nanocrystal. These measurements were performed at Brookhaven National Laboratory using a Hitachi HD2700C (200kV) with a probe aberration-corrector. Samples were prepared from a single drop of dilute nanoparticles in hexane deposited onto a copper grid coated with an ultrathin carbon (<3nm) / holey support film.

Inductively Coupled Plasma – Optical Emission Spectroscopy (ICP-OES)

ICP-OES measurements quantify the elemental composition of metallic and metal oxide nanoparticles. These compositional characterizations of our catalysts are conducted by ICP-OES using an in-house Perkin Elmer Avio 200.

X-ray Diffraction (XRD)

XRD measurements reveal the lattice pattern of a crystalline sample, used for confirmation of physical parameters pertinent to the study of nanocrystals. An X-ray is diffracted from a crystal surface and the angle at which the diffracted photon is detected is used to quantify the spacing between repeating lattice units. X-ray diffraction measurements were taken on a D/Max RA, Rigaku Co. instrument with Cu Kα radiation at a scanning rate of 4° per minute in the 2θ range of 30-80°.

1.3 Synthesis and Characterization of Aluminum-doped Zinc Oxide Nanocrystals

Unpublished work from my graduate research serves as a good example of two-metal-containing nanoparticles synthesized with optimized morphology using a solution-phase approach. We produced a simple synthetic scheme for monodispersed tetragonal aluminum-doped zinc oxide (AZO) nanocrystals with average 15 nm edge lengths. The synthesis procedure for AZO nanoparticles is based upon a previously reported method to obtain zinc oxide, with some modifications.[16] Figure 1.3 provides a collection of electron microscopy images of the AZO samples, which were characterized by transmission electron microscopy (TEM), high-resolution transmission electron microscopy (HRTEM), scanning transmission electron microscopy – electron energy loss spectroscopy (STEM-EELS), scanning electron microscopy – elemental dispersive spectroscopy (SEM-EDS), and inductively coupled plasma – optical emission spectroscopy (ICP-OES).

AZO nanocrystals with a Zn to Al precursor mole ratio of 4:1 were synthesized by the following method. 8 mL of 1-octadecene (ODE) and 0.46 mL of oleic acid (OAc) were degassed in a four-neck flask by vacuum evacuation on a Schlenk line for 1 hour at 90°C. Next, nitrogen gas was blanketed on the system and the temperature was increased to 275°C. Metal precursor solution was prepared in a N_2 glovebox by adding 0.4 mmol of diethylzinc and 0.1 mmol of triethylaluminum (0.5 mmol total metal) into 6 mL of trioctylphosphine. At room temperature, 0.66 mL of the stock solution was transferred out of the glovebox in a syringe and quickly injected into the reaction flask at 275°C. Immediately after the first injection, 1 mL of 1-undecanol was also injected into the reaction mixture. The temperature of the reaction mixture decreased to 250°C after the injections and was then increased to 270°C at about 5°C per minute. Ten minutes after the second injection, the heating mantle was removed, and the flask and its

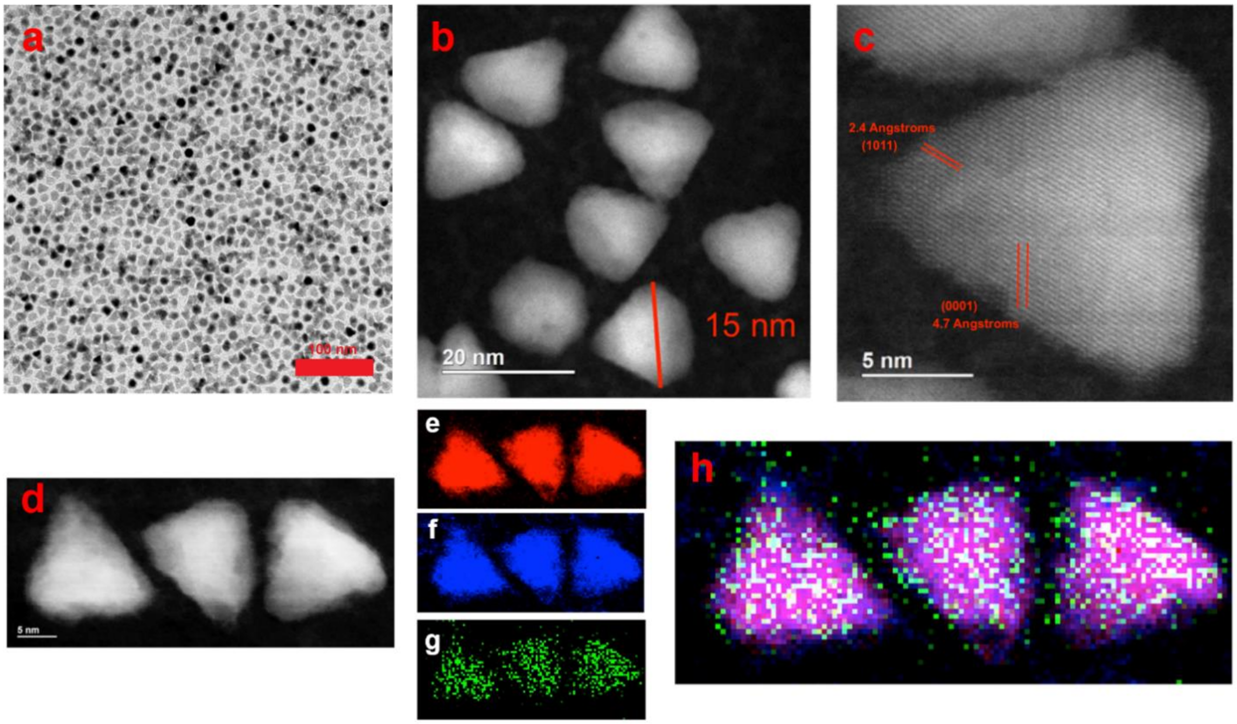

Figure 1.3. Aluminum-doped Zinc Oxide (AZO) nanoparticles with Zn to Al atomic ratio of 6:1 visualized by (a) TEM (scale bar is 100 nm), (b, c) HRTEM, and (d-h) STEM-EELS (scale bar is 5 nm).

contents cooled to room temperature. Colloidal nanoparticle products were precipitated from the reaction solution by addition of 70 mL 2-propanol and collected by centrifugation at 8000 rpm for 8 minutes. The resulting solid was dispersed in 5 mL hexanes and washed once more in 40 mL 2-propanol. The final products were stored in hexane as a stable dispersion. To prepare samples with different extents of aluminum doping, we varied the molar ratio of Zn(ethyl)$_2$ and Al(ethyl)$_3$ in the stock solution.

Structural characterizations were performed by low-resolution and high-resolution transmission electron microscopy. For each sample of AZO, we observed monodispersed nanocrystals with edge length of about fifteen nanometers, as shown in figures 1.3(a) and 1.3(b).

The bright field TEM image 1.3(a) shows that each particle grew to nearly identical size and shape, indicating that nucleation and growth of the crystals occurred within a narrow time window. This can be explained by rapid decomposition of ethylated precursors upon injection into the reaction solution, immediately followed by introduction of an alcohol species, leading to the controlled growth of individual, Al-doped ZnO particles without the formation of new crystalline nuclei. The HRTEM dark field image in figure 1.3(c) displays the lattice structure of the AZO nanocrystals, which have a tetragonal shape with truncated corners. The [0001] plane spacing was measured at 4.7 angstroms, and the [1011] plane spacing was measured at 2.4 angstroms.

The elemental compositions of the AZO nanocrystals were measured by ICP-OES to determine the extent of doping achieved from varied amounts of zinc and aluminum being present during the synthesis. These characterizations confirm that aluminum is incorporated into AZO nanoparticles at levels correlated to how much of each metal precursor is included in the stock solution. The spacial distribution of aluminum atoms within each AZO nanoparticle was resolved by STEM-EELS. Figure 1.3 shows (d) a STEM image of the AZO nanocrystals with elemental mappings for Zn (e), O (f) and Al (g) overlaid separately, along with (h) a composite image of all three EELS mappings. It is clear from the composite image that aluminum atoms are distributed homogenously throughout each nanoparticle.

1.4 References

1 Jarvie, H., King, S., Dobson, P., *Encyclopedia Britannica*, **2019**, https://www.britannica.com/science/nanoparticle.

2 Begley, M. R., Gianola, D. S., Ray, T. R., *Science*, **2019**, *364*, eaav4299.

3 Novoselov, K. S., Geim, A. K., Morozov, S. V., Jiang, D., Zhang, Y., Dubonos, S. V., Grigorieva, I. V., Firsov, A. A., *Science*, **2004**, *306*, 666-669.

4 Bonaccorso, F., Sun, Z., Hasan, T., Ferrari, A. C., *Nature Photonics*, **2010**, *4***,** 611–622.

5 Zang, J., Ryu, S., Pugno, N., Wang, Q., Tu, Q. Buehler, M. J., Zhao, X., *Nature Materials*, **2013**, *12*, 321–325.

6 Dai, X., Zhang, Z., Jin, Y., Niu, Y., Cao, H., Liang, X., Chen, L., Wang, J., Peng, X., *Nature* **2014**, *515*, 96-99.

7 Kim, T., Kim, K. H., Kim, S., Choi, S. M., Jang, H., Seo, H. K., Lee, H., Chung, D. Y., Jang, E., *Nature*, **2020**, *586*, 385-389.

8 Won, Y. H., Cho, O., Kim, T., Chung, D. Y., Kim, T., Chung, H., Jang, H., Lee, J., Kim, D., Jang, E., *Nature*, **2019**, *575*, 634-638.

9 Nagaoka, Y., Tan, R., Li, R., Zhu, H., Eggert, D., Wu, Y. A., Liu, Y., Wang, Z., Chen, O., *Nature*, **2018**, *561*, 378-382.

10 Yang, C. H., Leon, R. C. C., Hwang, J. C. C., Saraiva, A., Tanttu, T., Huang, W., Camirand Lemyre, J., Chan, K. W., Tan, K. Y., Hudson, F. E., Itoh, K. M., Morello, A., Pioro-Ladrière, M., Laucht, A., Dzurak, A. S., *Nature*, **2020**, *580*, 350-354.

11 Nelidova, D., Morikawa, R. K., Cowan, C. S., Raics, Z., Goldblum, D., Scholl, H. P. N., Szikra, T., Szabo, A., Hillier, D., Roska, B., *Science*, **2020**, *368*, 1108-1113.

12 Rolison, D. R., *Science*, **2003**, *299*, 1698-1701.

13 Chen, M. S., Goodman, D. W., *Science*, **2004**, *306*, 252-255.

14 Chen, P. C., Liu, X., Hedrick, J. L., Xie, Z., Wang, S., Lin, Q. Y., Hersam, M. C., Dravid, V. P., Mirkin, C. A., *Science*, **2016**, *352*, 1565-1569.

15 La Mer, V. K., *Industrial & Engineering Chemistry*, **1952**, *44*, 1270-1277.

16 Park, J., Zheng, H., Jun, Y. W., Alivisatos, A. P., *Journal of the American Chemical Society*, **2009**, *131*, 13943-13945.

Chapter 2

Introduction to Sustainable Electrocatalysis and Applications of Bimetallic Nanoparticles

2.1 Background on Catalysis

Catalytic systems are an integral part of our natural and industrial world. Enzymes are biological catalysts widely present in the cells of plants and animals.[1] Everyday materials (i.e., plastics) and chemicals are synthesized in enormous quantities by processes employing commercialized catalysts in specialized factory settings.[2] Metal elements serve as the active site, or primary chemical component of most catalysts due in part to their natural abundance, and in part to the size and shape of the d orbitals. Compared to s and p orbitals, more bonding and antibonding configurations are available with the d orbital orientations, such that a molecule adjacent to a metal site has more spacial possibilities to participate in the electronic interactions that take place during a catalytic process. Organic chemists routinely employ metal catalysts to make selective modifications to specific functional groups on large molecules, and some organometallic and nanomaterials chemists carefully study the preparation and behavior of metal catalysts.

A catalytic system is one in which a catalyst species lowers the activation energy for the chemical transformation of another species, called the substrate.[3] This occurs by chemisorption of a substrate molecule at a catalyst active site, which causes changes to the substrate's electronic structure local to the binding site. The substrate then undergoes a catalytic transformation(s) that would not occur if it were not bound to the catalyst, reacting on its own or with some other nearby chemical species, ultimately evolving into a product which desorbs from the catalyst. The catalyst is in the same chemical state at the start and finish of the process, regardless of how many steps may take place in between. Each reaction step occurs at a rate determined by a complex assortment of situational factors in the reaction environment, and optimization of these steps is how nature and the scientific community have both developed impressively efficient catalysts. The study of chemical kinetics, or the rates of chemical reactions has played a crucial role in developing industrial catalysts.[3]

Catalytic systems can be broadly classified into two types: homogenous and heterogenous. In homogenous catalysis, the catalyst and the substrate are in the same state of matter for the duration of the process. For example, a catalytic process would be considered homogenous if it took place entirely in the liquid phase, with a metal ion or small inorganic molecule as catalyst dissolved in a solvent along with the substrate species.[4] Heterogenous catalysis pertains to the alternative, where substrate and catalyst are in different phases. This is the case, for instance, in the catalytic converter of a car, where toxic fumes in engine exhaust are passed over a solid, precious metal catalyst and converted into less harmful gases.[5] Both homogenous and heterogenous catalysts have distinct advantages, but an especially prevalent factor contributing to the widespread presence of heterogenous catalysts in industry is the physical separation of catalyst and product. Product collection and catalyst recovery are easy when these species are in different states of matter, but separation tends to require more effort in a homogenous system.

Heterogenous catalysis takes place at the surface of a solid material, so the structure and composition of the catalyst material determines reaction behaviors. The number of catalytic reactions that can occur over some time is limited by the number of active sites, and section 1.1 introduced how the greater surface area / volume ratio of nanoparticles provides an atom utilization advantage over a bulk counterpart. Additionally, different surface sites like edges, corners, steps, etc. will interact differently with adsorbates, so to develop a better catalyst, one type of site might be synthetically expressed in preference to others.[6] The type of metal atom(s) making up the active surface also plays a significant role in terms of how the catalyst will interact with substrates and products. In general, the Sabatier principle can be used to correlate the adsorption / desorption properties of a substrate to the productivity of the catalyst species. Figure 2.1 summarizes how a best catalyst will exhibit substrate binding neither too weak nor too strong, allowing the substrate ample time and binding energy for transformation into the product, but also releasing the product once it is generated, making a surface site available for a new reaction.[7]

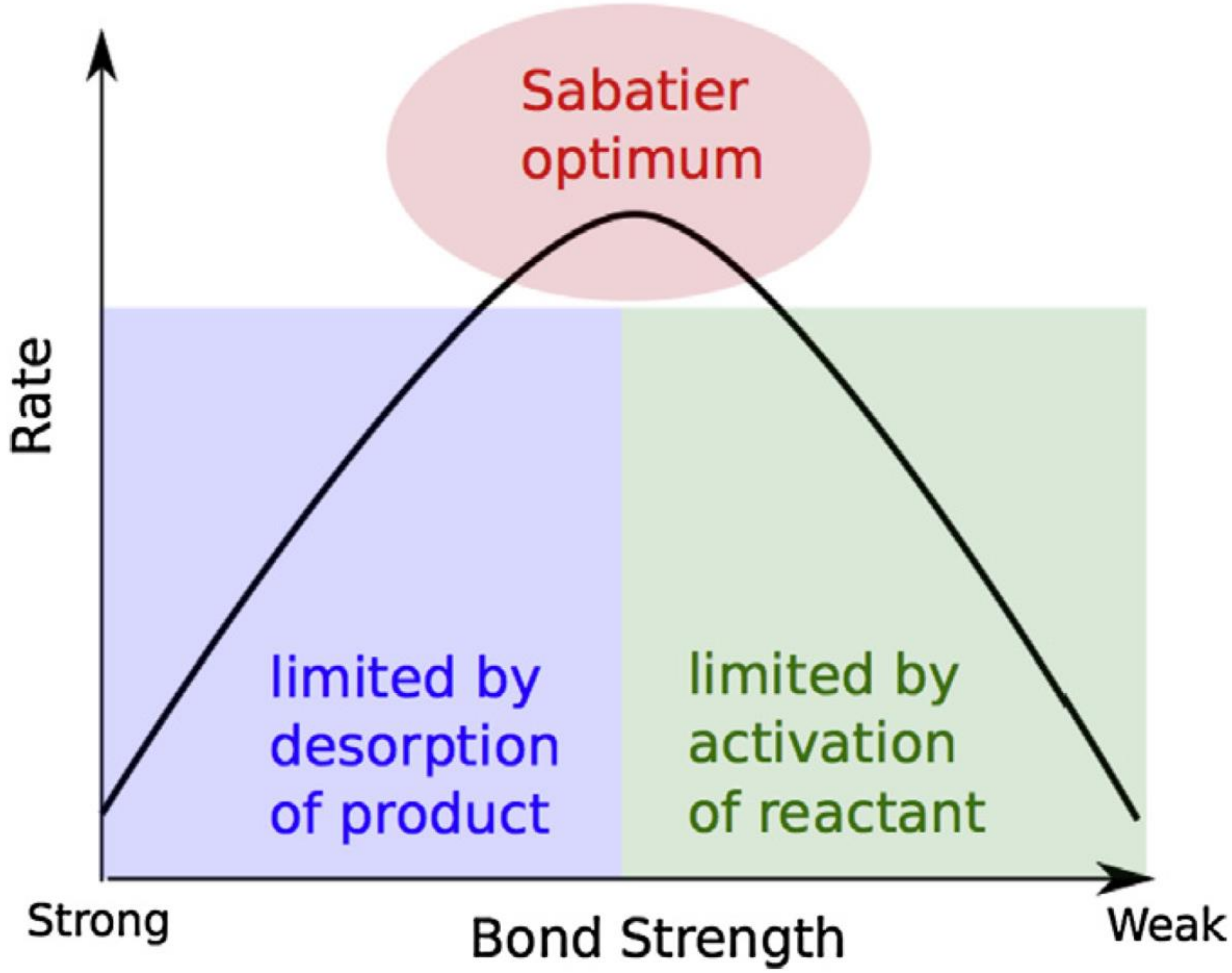

Figure 2.1. Simple representation of the Sabatier principle in heterogenous catalysis. Adopted from Medford *et al.*, 2015.[7]

2.2 Introduction to Electrocatalysis and Applications of Metal Nanoparticles

Electrochemistry is the fundamental design principle for various present-day energy technologies that can be used to power large electric devices, including vehicles.[8] A galvanic electrochemical cell (e.g. batteries, fuel cells) will discharge spontaneously when its electrodes are connected by an external circuit, converting chemical energy into electrical energy by oxidation at the anode surface and reduction at the cathode. An electrolytic cell uses an input of electricity to drive nonspontaneous redox reactions at the electrodes. Electrocatalysis is an important consideration in constructing any type of electrochemical cell, and this technique has some enticing advantages as an alternative to fossil fuel combustion or high temperature / pressure catalytic processes.[9] Much electrocatalysis is performed in a benign, low temperature environment. Aqueous electrolysis, where water might serve as an ion-transport medium or as a direct participant in surface chemistry, can be used to synthesize fuels and value-added chemicals with only electricity as a power supply, which could be acquired from renewable sources like solar, or wind. Furthermore, any gaseous waste from an electrochemical cell is usually a clean stream, unlike the fumes from a combustion engine.

When an electrolytic cell is subjected to sufficient applied potential, redox reactions are activated at the catalyst surfaces and ions migrate from one electrode to the other in a manner that balances the charge of moving electrons.[10] Experiments that scan (cyclic voltammetry, CV) or hold steady (controlled potential electrolysis, CPE) the potential of an electrochemical cell can be used to understand unique behaviors of different catalysts. To measure the electrochemical cell potential, a reference electrode is positioned near the working electrode, where electric potential is applied by the potentiostat instrument. The potential measured at the working electrode for a redox half reaction (1) can be thermodynamically related to the concentration of reactants using the Nernst Equation (2), shown below.[10]

$$O + ne \rightleftharpoons R \qquad (2.1) \qquad\qquad E = E^{0'} + \frac{RT}{nF}\ln\frac{[O]}{[R]} \qquad (2.2)$$

$E^{0'}$ is the standard thermodynamic potential for the reduction reaction as measured against the reversible hydrogen electrode. *R* is the ideal gas constant, *T* is the temperature, *n* is the electron transfer coefficient, and *F* is Faraday's constant. *[O]* and *[R]* are the concentration of oxidized and reduced species, respectively. The real potential of an electrocatalytic cell can be viewed as a complex summation of numerous half reactions at each electrode along with the considerations of kinetic pathways and of mass and charge transfer at interfacial junctions in the cell.

Metal nanoparticles have been studied as the active surface component on many types of electrodes. In a proton exchange membrane fuel cell (PEMFC), schematically depicted in figure 2.2, hydrogen gas (H_2) dissociates and adsorbs at an anodic catalytic surface, and protons migrate to the cathode through a semipermeable, hydrated polymer matrix called a proton exchange membrane.[11] Oxygen (O_2) from air is reduced by charge transfer at the cathodic catalyst surface, generating adsorbed oxygen intermediates that subsequently react with protons, finally desorbing as water. Electrons travel from anode to cathode through an external circuit, and a portion of this energy released from the anodic hydrogen oxidation reaction (HOR) can be used as electricity, while the rest provides the activation energy needed for the oxygen reduction reaction (ORR) at the cathode. It is worth noting that figure 1.1 is not mechanistically accurate, but detailed studies of the coordinated reactions in PEMFCs are available.[11] These reactions (HOR, ORR) and the reverse reactions often accompany aqueous electrochemistry where

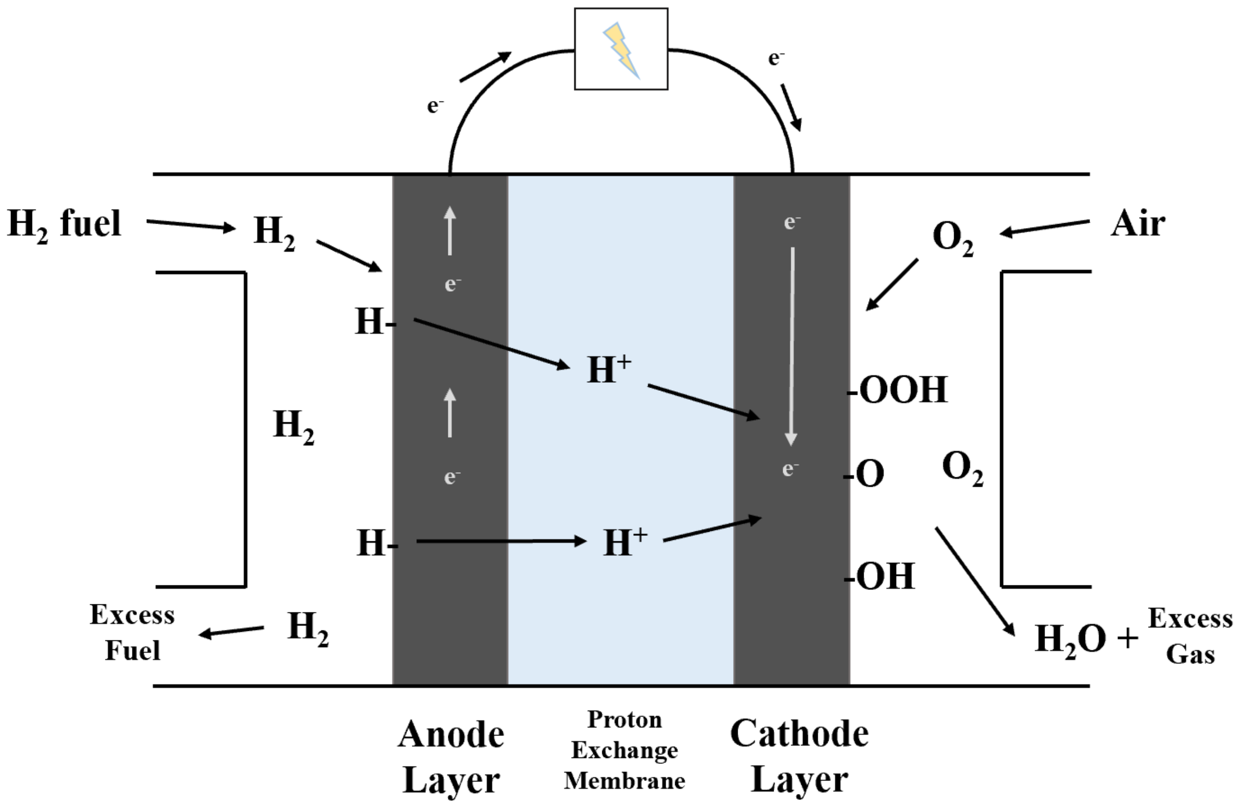

Figure 2.2. Schematic representation of a PEMFC.

heterogenous redox catalysis is used for driving selective chemical transformations of other molecules, as will be discussed in this chapter.

We can use electrochemistry to functionalize molecules that we currently emit as waste, or those we process using energy-intensive techniques, for example CO_2 or biomass.[12] Fuel cells contain entirely solid components, but more traditional electrochemical experiments utilize a liquid, oftentimes aqueous electrolyte. The electrolyte is some solution containing ions that will migrate and be consumed in electrochemical reactions when a potential is applied to the cell. Both solid electrodes are submerged in the electrolyte and connected to a potentiostat and one another by an external circuit. A substrate, the species of interest for catalytic conversion, is dissolved in the electrolyte and a programmed experiment adds specified amounts of electrical energy to the system, activating electron-transfer reactions at the electrode surfaces involving the substrate. Those reactions include chemisorption of the substrate to the cathode surface, surface chemistry reactions with other adsorbates, and desorption of product species into the electrolyte. The dynamics of those reactions depends on the nature of the catalyst surface, so much research in nanoparticle electrocatalysis wants to learn which metal surfaces optimize the catalytic conditions for producing a desirable chemical.[12] Electrocatalysts in CO_2RR are selected for generating a certain product among numerous possibilities, some of the most interesting being formic acid, methanol, and ethylene.[13] Section 2.4 will focus on the CO_2 reduction reaction (CO_2RR) as a main example of electrocatalysis.

Bimetallic nanoparticles can be viewed as a tool for tuning productivity and/or selectivity in electrocatalysis.[14] A surface comprised of two different metallic atoms will exhibit different binding to any reaction substrate compared to the monometallic counterparts. Competing reactions might be limited by energetically moderating the coverage of reactants using a bimetallic composition, which might also sequester poisoning species that bind too tightly on a monometallic surface. Special electronic effects of alloys can be utilized to identify a surface composition that optimally interacts with reaction intermediates. Our research group did just this in studying bimetallic AgPd nanoparticles for the electrocatalytic hydrodechlorination (EHDC) of 2,4-dichlorophenol (2,4-DCP) into phenol.[15] Figure 2.3 summarizes the findings of that publication, which bears my name as an author for my contributions to written language revisions. Figures 2.3(a) and 2.3(b) show that $Ag_{32}Pd_{68}$ nanoparticles performed better for EHDC than other alloy compositions, and better than pure Pd and Ag. Monometallic Pd outperformed Ag and Ag-dominant alloys, but this report discussed how incorporating a small amount of Ag into the Pd surface will raise its d-band center, alleviating over-strong adsorption of the product phenol. Alternatively, a majority Ag surface does not bind 2,4-DCP strongly enough for catalysis to proceed as effectively as on Pd. This Sabatier-type balancing relationship is drawn out schematically in figure 2.3(c).

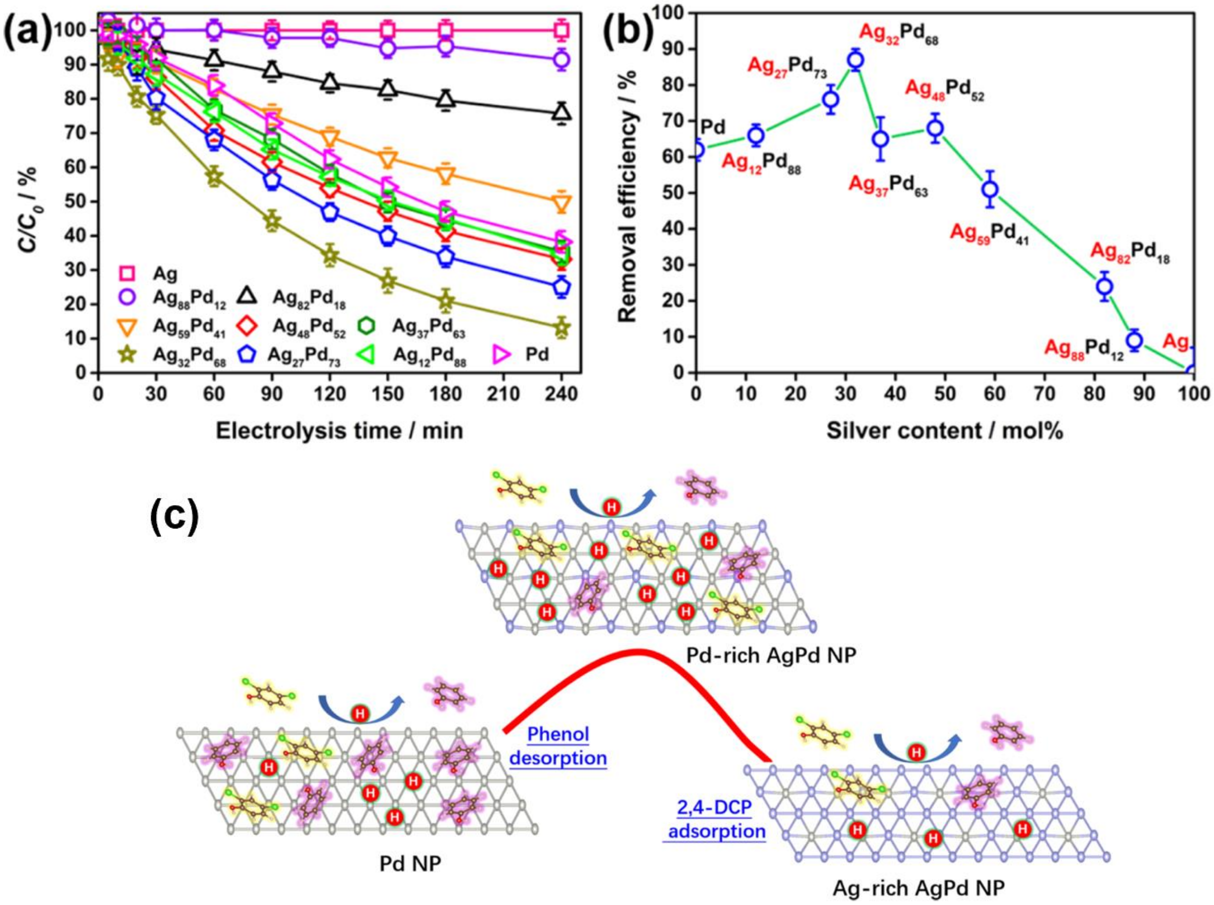

Figure 2.3. (a) EHDC performance of AgPd catalysts over time and (b) final removal efficiency correlated to the silver content in AgPd alloy nanoparticles. (c) Representation of catalyst surface activity related to alloy composition. Adopted from Peng & Cui *et al*., 2019.[15]

Approaches to electrocatalysis are diverse, and so are the types of metal nanoparticles catalysts that researchers might explore for a given transformation. Nanocrystal shapes and compositions can be synthetically expressed and compared, and when making comparisons of nanoparticle qualities in electrocatalytic conditions, morphological stability must be a significant consideration.[12] Nanocrystals do not necessarily retain their size and shape when supplied with energy at an electrode surface. Surface atoms on a nanoparticle generally have high surface energy, and after bearing an applied potential, as in the experiments described here, metal aggregation and structural change are common observations. For studies that compare the performance of catalyst nanoparticles based on their size, shape, or composition, the structure of the catalyst should be visualized after use in electrocatalysis studies to verify a consistent surface environment. If the surface changes during the experiment, it becomes hard or impossible to draw any reliable conclusions about the origins of catalytic activity without the use of *in-situ* characterization. Furthermore, long term stability would likely be a requirement for an economically efficient nanoparticle electrocatalyst in industry. TEM imaging of physical morphology can be sufficient evidence in some cases, but more detailed surface composition characterizations like X-ray spectroscopy are helpful tools to analyze the chemical nature of a surface.

2.3 Experimental Setup – H-cell for Electrocatalysis

The electrocatalytic experiments described in chapter 3 of this work used a two-chamber cell known as an “H-cell.” A picture of a typical H-cell setup is shown in Figure 2.4. A proton exchange membrane (Nafion 212) separates the two chambers. The cathodic chamber is sealed and purged of air with inert gas (N_2) or substrate gas, as in the case of CO_2 reduction reaction (CO_2RR). Gas flow out is coupled to a gas chromatographer to quantify the hydrogen (H_2)

evolution reaction (HER) that occurs at some metal cathodes. The cathodic chamber also contains a stirring bar, a working electrode, and a silver / silver chloride electrode. The anodic chamber contains a platinum mesh electrode.

There are different types of working electrodes conventionally used for H-cell catalysis experiments, but across the board, there are some steps that must be taken to fabricate a working electrode from a solution of colloidal metal nanoparticles. The surfactant molecules covering the surface of the nanoparticles stabilizes them from agglomeration during and after the synthetic reaction, but these ligands must be removed to expose metal surface sites that participate in catalysis. To prepare an electrode with morphologically-sound and ligand-free nanoparticles, the nanoparticles must be deposited onto some conductive material with high surface area, and then stripped of the surfactant. Carbon materials are commonly used as the nanoparticle support in electrocatalytic experiments; dissolved nanoparticles are deposited onto the carbon surface by physical mixing with carbon in nonpolar solvent and aggravation in a sonication bath. Once nanocrystals are evenly distributed and immobilized on the support surface, some treatment is performed to remove the organic outside layer from the nanoparticles. Chemical treatments such as acid washing are common for surfactant-removal, as are heating methods for calcination. Washing methods might be preferable for nanoparticles applied in room temperature electrocatalysis experiments as to avoid the coking possibility under high temperature treatment conditions. Finally, the nanoparticle-carbon catalyst materials are spray-coated onto conductive carbon paper (black strip in cathode chamber in figure 2.4) or drop-cast onto a glassy carbon rod at a known amount for use as the electrode. Carbon paper is used in this report for the advantage of higher catalyst loading.

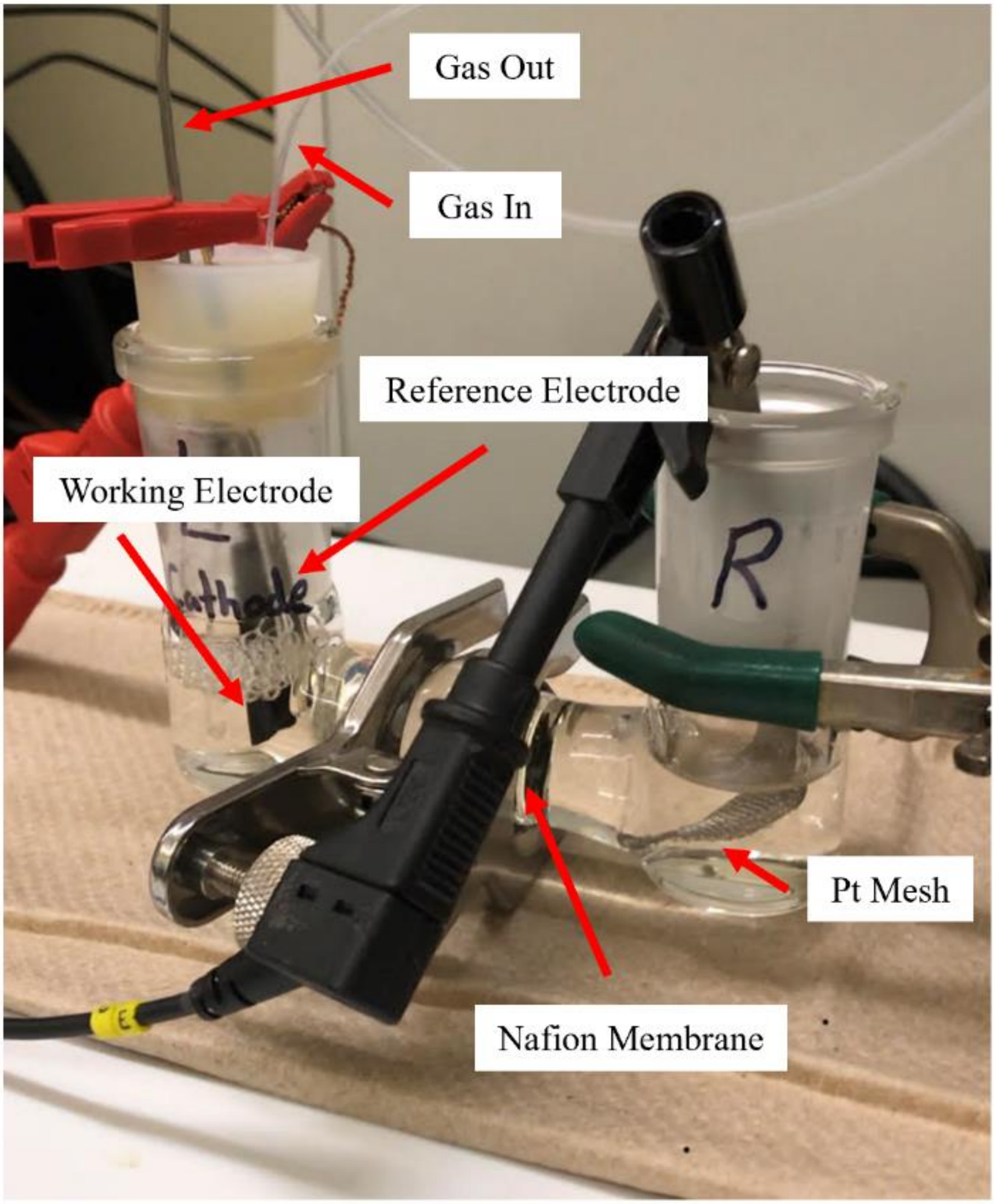

Figure 2.4. Typical H-cell setup for electrochemical experiments described in chapter 3 of this work.

Some common electrochemistry experiments can be used to characterize the performance of an electrocatalyst.[10] When enough electrochemical potential is applied to the working electrode, the substrate species begins to react at the catalyst surface, transforming into a product and desorbing back into the electrolyte. The relevant reactions will occur at a higher rate when greater overpotential is applied. Experiments that manipulate the applied potential over time can give insight into the catalytic reaction capabilities of a given catalyst. Cyclic voltammetry (CV) experiments are used to evaluate the behavior of a catalyst over a range of potentials. The magnitude of the applied potential is scanned at a designated rate and plotted against the amount of current, which is related to the rate of the chemical reactions at the electrode surface. Controlled potential electrolysis (CPE) experiments are useful experiments to measure reaction performance metrics like productivity and selectivity. As opposed to CV, the applied potential is held steady for the duration of a CPE experiment, during or after which the electrolyte and gaseous headspace can be collected and analyzed for the electrocatalytic substrate conversion, product yields, and current efficiencies. Used together, CV and CPE can provide the basic data for contributive studies in the field of nanoparticle electrocatalysis.

This work explores nanoparticle catalysts fabricated into working electrodes that test the electrocatalytic properties of nanoparticles for green chemical conversions. Interest here is focused on the cathodic reaction, so we place the reference electrode nearby, in the same chamber. The oxygen (O_2) evolution reaction (OER) occurs at the anodic Pt surface. Under sufficient applied potential, water in the electrolyte is oxidized and splits into protons and hydroxide anions, and the protons migrate to participate in the cathodic reaction. OER is not a focal point of consideration in our electrocatalytic reduction studies, but there is a wealth literature exploring the best catalysts and mechanisms for OER.

2.4 Bimetallic Nanoparticles for Electrocatalytic Reduction of CO_2

Carbon dioxide is a leading topic of discussion regarding warming climates around the globe due to its large, growing concentration in the atmosphere and its behavior as a greenhouse gas. Much research has been conducted in pursuit of efficient and active catalytic methods for converting CO_2 into more useful products, with electrocatalytic reduction emerging as a sustainable and clean solution with high potential for development.[4] This section will introduce the electrocatalytic CO_2 reduction reaction (CO_2RR), then use it as a context for discussing rational design of nanoparticle catalysts.

Electrocatalytic CO_2RR has been reported for CO_2 conversion into a variety of other small molecules, some of which are shown in table 2.1 alongside their respective half reactions and thermodynamic potentials in acidic and alkaline electrolyte.[16] The listed CO_2RR products are all desirable as opposed to wasted CO_2, and the literature contains examples of reports designed in pursuit of each of those products independently. Hydrogen evolution reaction (HER) competes at the cathode against CO_2RR when the desired carbon product is hydrogenated, but H_2 can also be targeted to accompany CO synthesis since the combined gas mixture is syngas. Formic acid and methanol are used as chemical intermediates and solvents, and methane from CO_2RR has clear advantages to natural gas. Ethylene is a highly desirable product of CO_2RR, in part due to its use in polyethylene synthesis, with copper being the most noteworthy catalyst for ethylene production from CO_2 electroreduction.

It is worth noting that table 2.1 only considers the thermodynamics of the electrocatalytic reactions summarized, which each take place in a complex sequence of steps involving each participant, and the potential values calculated are only standardized representations of the net equilibrium energy of the process. A real electrocatalytic reaction in a practical system involves

Product	**Acid Half Reaction**	**E (V)**	**Base Half Reaction**	**E (V)**
Hydrogen (H_2)	$2H^+ + 2e^- \rightarrow H_2$	0.000	$2H_2O + 2e^- \rightarrow H_2 + 2OH^-$	-0.828
Carbon Monoxide (CO)	$CO_2 + 2H^+ + 2e^- \rightarrow CO + H_2O$	-0.104	$CO_2 + H_2O + 2e^- \rightarrow CO + 2OH^-$	-0.932
Formate / Formic Acid ($HCOO^-$ / HCOOH)	$CO_2 + 2H^+ + 2e^- \rightarrow HCOOH$	-0.171	$CO_2 + H_2O + 2e^- \rightarrow HCOO^- + OH^-$	-0.639
Methanol (CH_3OH)	$CO_2 + 6H^+ + 6e^- \rightarrow CH_3OH + H_2O$	0.016	$CO_2 + 5H_2O + 6e^- \rightarrow CH_3OH + 6OH^-$	-0.812
Methane (CH_4)	$CO_2 + 8H^+ + 8e^- \rightarrow CH_4 + 2H_2O$	0.169	$CO_2 + 6H_2O + 8e^- \rightarrow CH_4 + 8OH^-$	-0.659
Ethylene (C_2H_4)	$2CO_2 + 12H^+ + 12e^- \rightarrow C_2H_4 + 4H_2O$	0.085	$2CO_2 + 8H_2O + 12e^- \rightarrow C_2H_4 + 12OH^-$	-0.743

Table 2.1. CO_2 reduction reaction possible products, overall half reactions to give those products in acid and base electrolyte, and the standard thermodynamic redox potentials. Adopted from Fan *et al.*, 2020.[16]

electron-transfer steps, catalyst-substrate interactions, substrate-substrate interactions, movement of those species within the electrochemical double layer and at the catalyst surface, and other nontrivial moving parts that require additional energy input beyond what is described by the standard potential. This energy, referred to as the overpotential, can be attributed to kinetic features of the system and is a key benchmark for the performance of a catalyst, assuming cell setup to be held constant.[10]

Figure 2.5, adopted from a theoretical study of electrocatalytic CO_2RR, helps to visualize the concept of overpotential.[17] The simplified reaction mechanism in 2.5(a) depicts CO_2RR to generate methane using a Cu catalyst in acidic electrolyte, where CO_2 is first reduced,

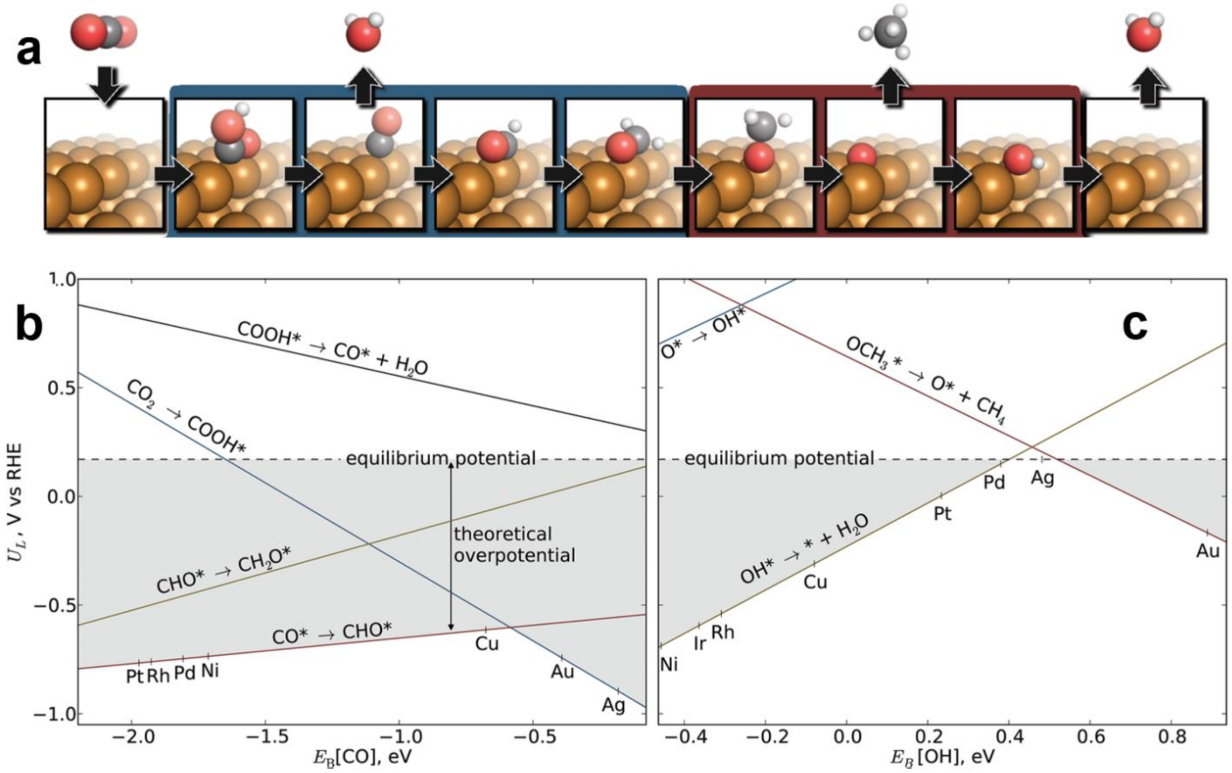

Figure 2.5. (a) A proposed mechanism for CO_2 electroreduction to CH_4 on Cu *fcc* (211) surface. (b, c) Limiting potentials (U_L) for the reactions in the mechanism plotted against the catalyst binding affinity to (b) CO and (c) OH. Adopted from Peterson and Nørskov, 2012.[17]

hydrogenated, and adsorbed to generate *COOH. Keep in mind that this figure represents only one of numerous proposed pathways. In this example, that initial molecule remains adsorbed on the Cu surface and undergoes further electron transfer and hydrogenation steps, culminating in desorption of a methane molecule containing the same carbon atom that started in CO_2. Figures 2.5(b) and 2.5(c) plot the limiting potential (U_L), or the minimum applied potential to drive the forward reaction for most of the steps in 2.5(a), but based on other metal electrocatalysts along with Cu. The plotted U_L lines in figure 2.5(b) are dependent on the calculated binding affinity of the catalyst surface to the *CO intermediate. The latter reactions in figure 2.5(c) have their U_L calculated based on the affinity for *OH. The equilibrium potential for CO_2 to CH_4 conversion is the dotted line at 0.17 V vs. RHE, and the shaded areas highlight the overpotential, which here is visualized as the energy difference between the theoretical equilibrium potential and the actual energy required to activate the rate-limiting step, which is different on certain surfaces. The different metals studied are plotted in 2.5(b) and (c) at the most negative limiting potential calculated at the metal-adsorbate binding energy. The potential line on which each metal is plotted roughly represents the rate-limiting step for the overall CO_2 methanation using that catalyst. Looking at the metal-CO binding energies in 2.5(b), Ag and Au have weak binding to CO, while Pt, Pd, Rh and Ni interact strongly with the CO intermediate, and Cu has a more intermediate carbon affinity. The paper introduces how Au and Ag are good catalysts for CO production, whereas Cu can generate hydrocarbons, and Pt and Ni will generate H_2 with high selectivity. The plots in figure 2.5, particularly 2.5(b), provide rationale those observations from a few perspectives. CO generation by Au and Ag might be explained by the evidence that CO_2 to *COOH is the limiting step on those metals. *COOH is then converted to *CO and H_2O, and *CO has a high likelihood of desorption due to the weak binding affinity. Copper’s moderate binding energy set it at the tip of a volcano-type plot where it is shown to require lower overpotential than other metal catalysts for the *CO hydrogenation step. Carbon monoxide is implicated in the carbon-carbon coupling step required to generate multi-carbon products from CO_2, so Cu can be viewed as having a CO adsorption-desorption balance that prioritizes CO-CO coupling over hydrogenation. The overly strong carbon affinity of Ni, Pt, Pd and Rh might help to explain their limited generation of carbon products from CO_2RR because high coverages can be a hindrance during the reaction. In summary, this computational study serves as a good introduction to overpotential and kinetics in the context CO_2RR.

State of the art performances for CO_2RR are achieved by a combination of catalyst selection and cell design. Bimetallic nanoparticles can be difficult to study mechanistically due to the complexity of reaction participants and different surface sites, so some theoretical studies of CO_2RR focus on simpler surfaces in their pursuit of a reaction pathway, but these can be extended and applied by researchers who develop and test bimetallic surfaces in the laboratory. Metal alloying is one of many synthetic approaches for thwarting phenomenon like poisoning, tuning selectivity, and increasing catalytic activity. As has already been discussed, the local electronic environment of an absorbed substrate can be quite varied depending on the composition of the surface, and an alloyed surface will provide different, additional surface sites in comparison to the monometallic counterparts. Control over the alloy composition and structure can be utilized to modulate adsorbate binding behaviors, which in turn affects catalytic activity. As shown in figure 2.6(a-c), different phases of PdCu alloy nanoparticles displayed different activity as CO_2RR catalysts.[18] Ma *et al*. reported changes in catalyst behavior based on the alloy phase of PdCu nanoparticles, which was either ordered, disordered, or separated (fig. 2.6a). Mixed phases (ordered and disordered) showed better current efficiency to CO (fig. 2.6b), while the phase separated PdCu performed with good selectivity to ethylene: nearly 50% faradaic efficiency at -0.7 V vs. RHE (fig. 2.6c).

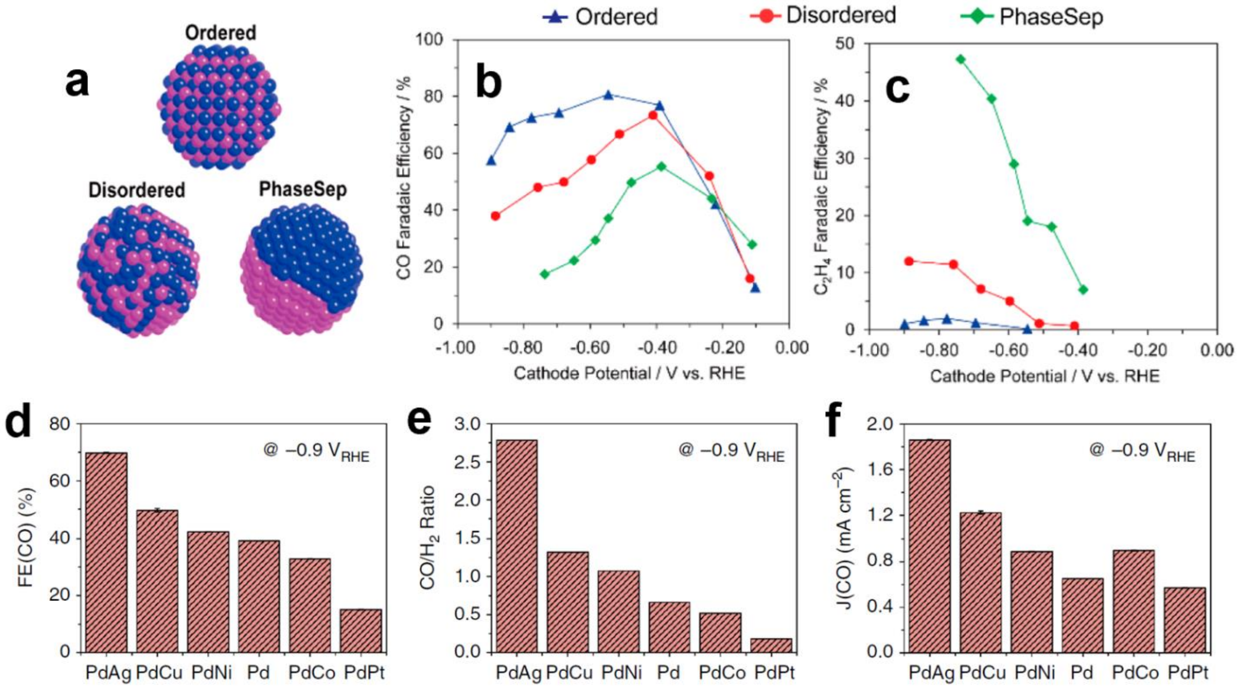

Figure 2.6. (a) Different phases of nanoparticles and their faradaic efficiency to (b) CO and (c) C_2H_4 in CO_2RR. Adopted from Ma *et al*. 2017.[18] (d-f) Syngas production information from CO_2RR using different Pd-M alloy nanoparticles. Adopted from Lee *et al.*, 2019.[19]

In the electrocatalytic reduction experiments depicted in this report, it is possible for HER to compete against desirable reactions at the cathode surface. Protons or adsorbed hydrides undergo addition to the substrate in most electrocatalytic reduction reactions, but at negative enough potentials, hydrides can interact together, bind, and desorb as H_2 gas. This reaction consumes a portion of the applied charge, which is unfavorable in scenarios where some product besides hydrogen is targeted. For this reason and others, HER is an important electrocatalytic reaction with a deep network of literature. Bimetallic nanoparticles might be used to tune hydrogen adsorption properties, as was reported for Pd-metal alloy nanoparticles in the electrocatalytic reduction of CO_2 into synthesis gas, an industrially vital mixture of CO + H_2.[19] Lee et al. reported M-Pd nanoparticles (M = Co, Ni, Cu, Ag, and Pt) (M:Pd mole ratio 1:4) by comparison for their CO_2RR performance, as summarized in figure 2.6(d-f), specifically for production of CO/H_2 in bicarbonate electrolyte. They found that AgPd had the highest CO selectivity and partial current density, and CuPd and NiPd produced a nearly balanced 1:1 CO/H_2 product while also maintaining good efficiency to CO.

Different cell and electrode types are used for certain applications. Kinetic studies in the present day sometimes use a rotating disk electrode which lowers the thermodynamic contribution of mass transfer at the catalyst surface. Carbon paper is a common choice for its high catalyst loading area, favorable for bulk electrolysis experiments. A reference electrode, of which there are many types, is selected in part for compatibility with the system chosen for study. A cell with two compartments can be preferable to one when it is necessary to physically separate the working and counter electrodes, maybe to prevent product migration and undesired reactivity. For an experiment looking to maximize current density, an electrocatalytic flow cell can be designed in such a way that fresh electrolyte and gaseous substrate are pumped along the electrocatalytic surface, improving mass transfer of species to and from the electrode.

Figure 2.7 shows a CO_2RR flow cell diagram and a general visualization of the reactions occurring at the catalyst surface in a gas diffusion electrode (GDE).[20] It is adopted from a series of publications in *Science* magazine from the group of Edward Sargent in which they study the production of ethylene from CO_2RR in a flow cell using a surface-modified copper catalyst. Figure 2.7(a) shows that the flow cell has two chambers separated by an anion (OH^-) exchange membrane. A customized gas diffusion electrode is used at the cathode to keep dry the gaseous substrate CO_2 as it travels to the catalyst / electrolyte interface, forming a triple-phase boundary where electrocatalytic reactions take place. The GDE / catalyst / electrolyte interface is represented by figure 2.7(b). Alkaline potassium hydroxide electrolyte is flowed along the catalyst surface, meeting the gas which emerges from the GDE. CO_2 will adsorb at the catalyst surface, participate in surface reactions, and then desorb into the gas or electrolyte flow as a product. Figure 2.7(c) also shows this process, detailing the occurrence of undesired reactions (i.e., HER) at metal sites to which CO_2 does not migrate. This is a persisting limitation in aqueous CO_2 electroreduction, the low solubility of CO_2, which limits the possibility of catalytic reactions to a small region close to the triple-phase boundary. Figure 2.7(d) visualizes the researchers' solution to the gas diffusion issue: they coated the copper surface with a bilayer of ionomer with a hydrophobic inner region along the metal surface, forming a channel through which CO_2 was able to diffuse unobstructed by interactions with the electrolyte, reaching metal sites that would otherwise have been rendered inaccessible by the electrolyte. As a result, large ethylene partial current densities above 1 A cm^{-2} with cathodic energy efficiencies above 40% were produced.

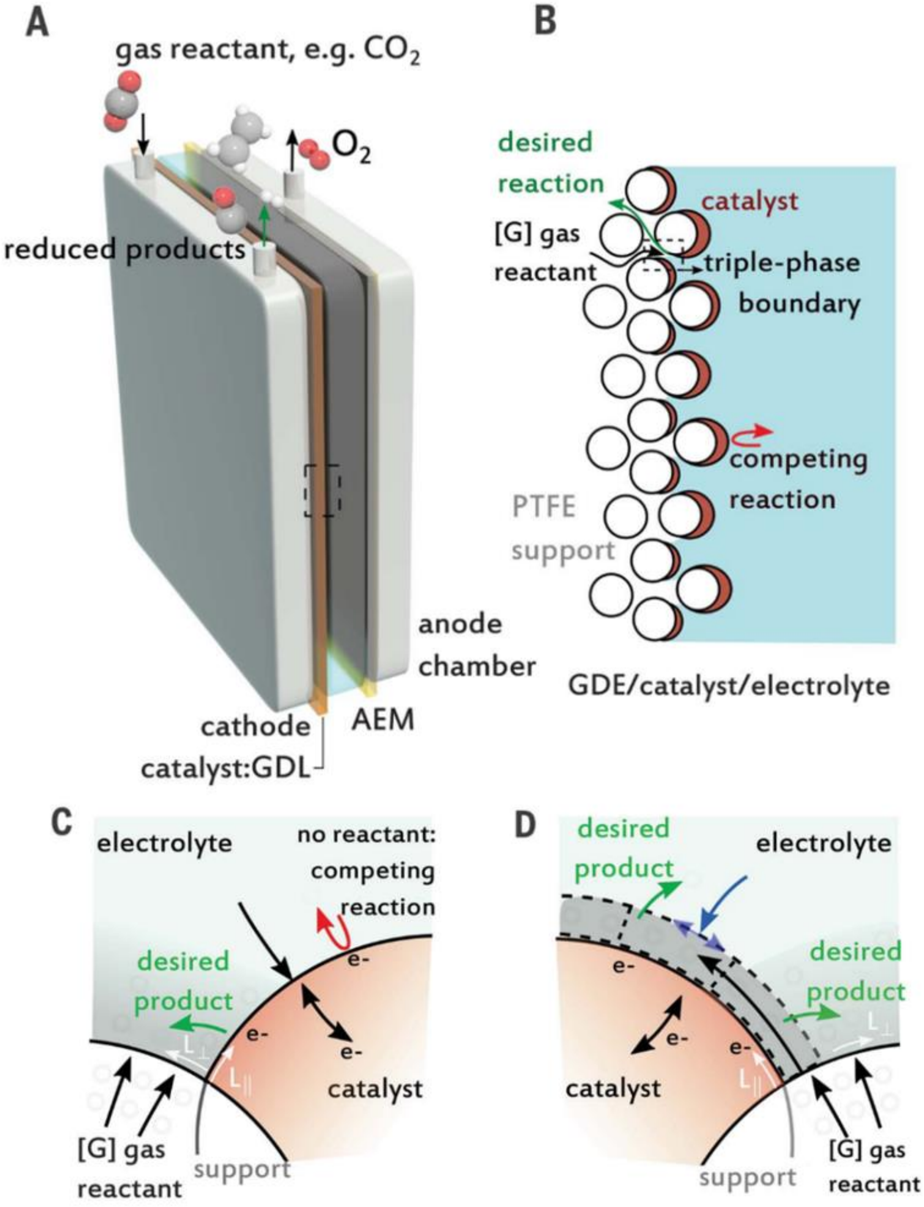

Figure 2.7. (a) Flow cell diagram for CO_2RR and (b) a generalized depiction of the GDE / catalyst / electrolyte interface. The bottom images are a more detailed image of the electrocatalytic interface (c) without and (d) with an ionomer layer for enhanced gas diffusion. Adopted from García de Arquer *et al.*, 2020.[20]

2.5 References

1 McKee, T. & McKee J.R., *Biochemistry: the Molecular Basis of Life*, **2012**, *5*, 182-225.

2 Armor, J. N., *Catalysis Today*, **2011**, *163*, 3-9.

3 Davis, M. E. & Davis, R. J., *Fundamentals of Chemical Reaction Engineering*, **2003**, *1*, 133-182.

4 Wang, W. H., Himeda, Y., Muckerman, J. T., Manbeck, G. F., Fujita, E., *Chemical Reviews*, **2015**, *115*, 12936-12973.

5 Farrauto, R. J., Deeba, M., Alerasool, S., *Nature Catalysis*, **2019**, *2*, 603-613.

6 Tian, X., Zhao, X., Su, Y. Q., Wang, L., Wang, H., Dang, D., Chi, B., Liu, H., Hensen, E. J. M., Lou, X. W., Xia, B. Y., *Science*, **2019**, *366*, 850-856.

7 Medford, A. J., Vojvodic, A., Hummelshøj, J. S., Voss, J., Abild-Pedersen, F., Studt, F., Bligaard, T., Nilsson, A., Nørskov, J. K., *Journal of Catalysis*, **2015**, *328*, 36-42.

8 Pomerantseva, E., Bonaccorso, F., Feng, X., Cui, Y., Gogotsi, Y., *Science*, **2019**, *366*, eaan8285.

9 De Luna, P., Hahn, C., Higgins, D., Jaffer, S. A., Jaramillo, T. F., Sargent, E. H., *Science*, **2019**, *364*, eaav3506.

10 Bard, A. J. & Faulkner, L. R., *Electrochemical Methods: Fundamentals and Applications*, **2001**, *2*.

11 Wang, X. X., Swihart, M. T., Wu, G., *Nature Catalysis*, **2019**, *2*, 578-589.

12 Seh, Z. W., Kibsgaard, J., Dickens, C. F., Chorkendorff, I., Nørskov, J. K., Jaramillo, T. F., *Science*, **2017**, *355*, eaad4998.

13 Álvarez, A., Bansode, A., Urakawa, A., Bavykina, A. V., Wezendonk, T. A., Makkee, M., Gascon, J., Kapteijn, F., *Chemical Reviews*, **2017**, *117*, 9804-9838.

14 Gilroy, K. D., Ruditskiy, A., Peng, H. C., Qin, D., Xia, Y., *Chemical Reviews*, **2016**, *116*, 10414-10472.

15 Peng, Y., Cui, M., Zhang, Z., Shu, S., Shi, X., Brosnahan, J. T., Liu, C., Zhang, Y., Godbold, P., Zhang, X., Dong, F., Jiang, G., Zhang, S., *ACS Catalysis*, **2019**, *9*, 10803-10811.

16 Fan, L., Xia, C., Yang, F., Wang, J., Wang, H., Lu, Y., *Science Advances*, **2020**, *6*, eaay3111.

17 Peterson, A. A. & Nørskov, J. K., *The Journal of Physical Chemistry Letters*, **2012**, *3*, 251-258.

18 Ma, S., Sadakiyo, M., Heima, M., Luo, R., Haasch, R. T., Gold, J. I., Yamauchi, M., Kenis, P. J. A., *Journal of the American Chemical Society*, **2017**, *139*, 47-50.

19 Lee, J. H., Kattel, S., Jiang, Z., Xie, Z., Yao, S., Tackett, B. M., Xu, W., Marinkovic, N. S., Chen, J. G., *Nature Communications*, **2019**, *10*, 3724.

20 García de Arquer, F. P., Dinh, C.T., Ozden, A., Wicks, J., McCallum, C., Kirmani, A. R., Nam, D. H., Gabardo, C., Seifitokaldani, A., Wang, X., Li, Y. C., Li, F., Edwards, J., Richter, L. J., Thorpe, S. J., Sinton, D., Sargent, E. H., *Science*, **2020**, *367*, 661-666.

Chapter 3

AgPd Nanoparticles for Electrocatalytic Reduction of Furfural with High Selectivity to Furfuryl Alcohol

3.1 Background and Motivation

Biomass could serve as a sustainable source of fuels and chemicals which currently come from nonrenewable fossil fuels.[1-3] Most plants contain structural cellular material referred to as lignocellulose, comprised of the biopolymers lignin, cellulose, and hemicellulose.[4] Wasted plant parts from the agricultural and logging industries can contain high quantities of lignocellulose, and there are existing industrial processes to break down this biomass into its constituent monomeric sugars, as well as to transform those into other useful molecules. Figure 3.1 shows xylose, a building block of hemicellulose which consists of chains of a variety of five- and six-membered sugar molecules. A large amount of industrial xylose is converted into furfural (2-furfuraldehyde),[5] which is processed into useful chemicals including furfuryl alcohol,

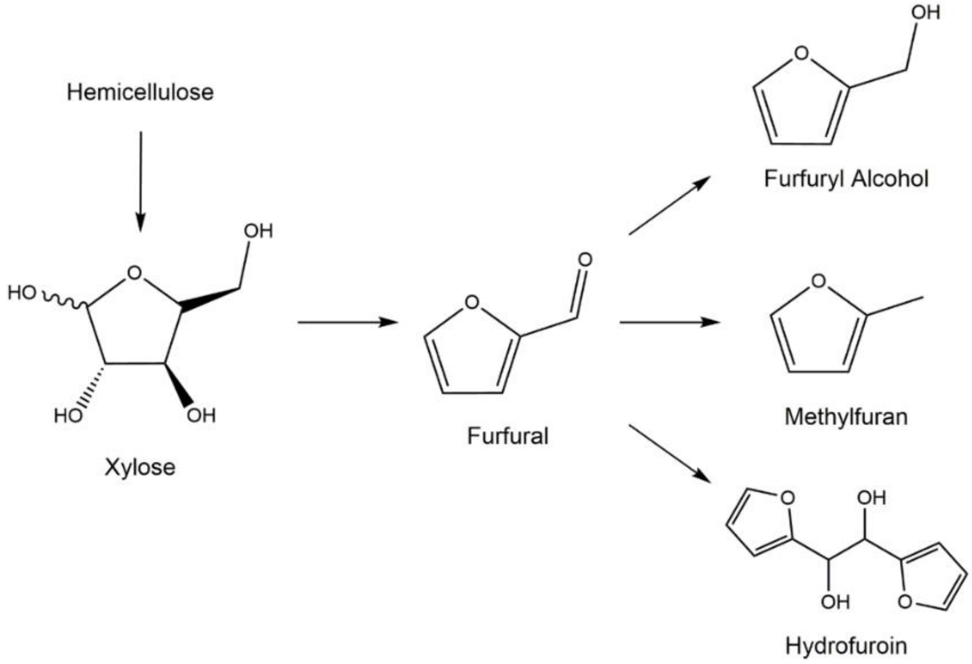

Figure 3.1. General pathway for furfural production and electrocatalytic reduction reaction product possibilities.

applied in textiles and chemicals, and methylfuran, a volatile biofuel.[6] Much of this chemistry is performed at high temperature and/or pressure, but electrocatalysis could serve as a replacement to more energy intensive technologies.[7]

Furfuryl alcohol is the primary value-added chemical produced from furfural in today's market,[8] so previous researchers interested in electrocatalytic reduction of furfural have chosen to target furfuryl alcohol, as we do in this report. Some trends are emerging in the field of furfural electroreduction that suggest different precious metal nanoparticles such as Pd, Pt, and Ru are suited for producing furfuryl alcohol, while Cu has been reported in association with methylfuran selectivity.[9] Neutral pH conditions have seen the highest reported selectivities to furfuryl alcohol, but this product can also be generated in acidic conditions. Methylfuran is limited to lower pH around 1, and furanics are unstable in basic conditions. Studies in neutral conditions are less common, and furfural electroreduction reports using monodisperse bimetallic nanoparticles did not exist before publication of the contents of this chapter in *Nanoscale,* so we hope our work will be a welcome contribution to a growing field. Table 3.1 provides some other reported catalysts for comparisons of conditions and catalytic performance.

This chapter describes the synthesis of alloy AgPd nanoparticles and their application for the electrocatalytic reduction of furfural. Previous studies from our lab group provide evidence that AgPd alloy nanoparticles can perform as better catalysts than their monometallic counterparts.[10] We suggest that this is due to an electronic effect where the binding energy of key reaction intermediates is tuned to a moderate level, and better catalytic performance is observed. In this work, we have synthesized a suite of AgPd alloy nanoparticles and determined that an atomic composition of $Ag_{60}Pd_{40}$ leads to the highest selectivity and yield to furfuryl alcohol in the electrocatalytic reduction of furfural. At low overpotentials, this catalyst performed at over 95%

selectivity and appreciable yield of 160 μmol h^{-1}, and all the alloy nanoparticles performed better than pure Pd and Ag counterparts.

Catalyst	**Electrolyte (pH)**	**Furfuryl Alcohol Yield**	**Faradaic Efficiency to Furfuryl Alcohol (%)**	**Ref.**
Cu-graphite	phosphate buffer (6.6)	N/A	95%	11
Cu foil	0.5 M sulfate (3)	65 umol h^{-1}	40%	6
Cu	0.2 M NH_4Cl	N/A	25%	9
Cu-DHP	0.5 M C_2H_5OK	N/A	60%	12
Pt	0.5 M H_2SO_4	N/A	60%	13
Pd	5wt% acetic acid; 47.5wt% isopropanol	4600 umol h^{-1}	N/A	14
Pd	0.5 M H_2SO_4	110 umol h^{-1}	30%	7
$Ag_{60}Pd_{40}$ nanoparticles	phosphate buffer (6.8)	160 umol h^{-1}	96%	This work

Table 2.1. Literature reports of furfuryl alcohol production from electrocatalytic reduction of furfural.

3.2 Results and Discussion

In this work, we prepared a set of monodisperse AgPd nanoparticle catalysts with controlled bimetallic compositions and applied them for the electrocatalytic reduction of furfural in neutral, aqueous electrolyte. The Ag was anticipated to promote Pd performance for furfural electrocatalytic reduction, as our previous studies revealed that Pd was subject to over-strong adsorption of aromatic entities and could be effectively modulated by Ag alloying.[10] The results herein demonstrate that bimetallic AgPd alloy nanoparticles performed with higher furfuryl alcohol selectivity and yield than monometallic Ag and Pd analogues at low overpotentials. Out of the catalysts with varied bimetallic compositions, $Ag_{60}Pd_{40}$ performed best at -0.4 V and -0.5 V vs. RHE. We employed this catalyst to further study the effects of electrolytes with different pH. These results suggested that neutral buffer provided an optimal environment for selective furfuryl alcohol production. Competition from HER was detrimental to furfuryl alcohol selectivity in acidic electrolytes.

The AgPd alloy nanoparticles were prepared by the co-reduction of Ag and Pd salts in a colloidal synthesis, using our previously reported method.[15] The nanoparticles were loaded onto a carbon support and the catalysts were treated with glacial acetic acid to remove bulky surface ligands for all electrochemical studies, as was also discussed in our previous report. We tuned the Ag/Pd atomic composition by controlling the precursor ratio and characterized it using ICP-OES. The calculated metal atom compositions (by atomic percentage) for the nanoparticles used to study alloy effects were $Ag_{75}Pd_{25}$, $Ag_{60}Pd_{40}$, $Ag_{50}Pd_{50}$, and $Ag_{30}Pd_{70}$. Metal loadings on the electrode surfaces were consistent at 0.6 mg_{metal} cm^{-2} across samples used in each set of experiments.

Figures 3.2(a-c) and figure 3.3 provide TEM images of as-synthesized Ag, Pd, and AgPd alloy nanoparticles, and figure 3.2(d) shows the carbon supported $Ag_{60}Pd_{40}$ catalyst after surface ligand removal. These samples are all comparable in size and shape, and the morphologies of the ligand-removed nanoparticle catalysts are uniform. Figure 3.4 shows TEM images of Ag, Pd, and $Ag_{60}Pd_{40}$ catalysts after use in constant potential electrolysis (CPE) experiments. It indicates that some nanoparticle agglomeration is visible under electrochemical conditions for the Ag, but Pd-containing nanoparticle catalysts are physically stable throughout employment in the system examined here.

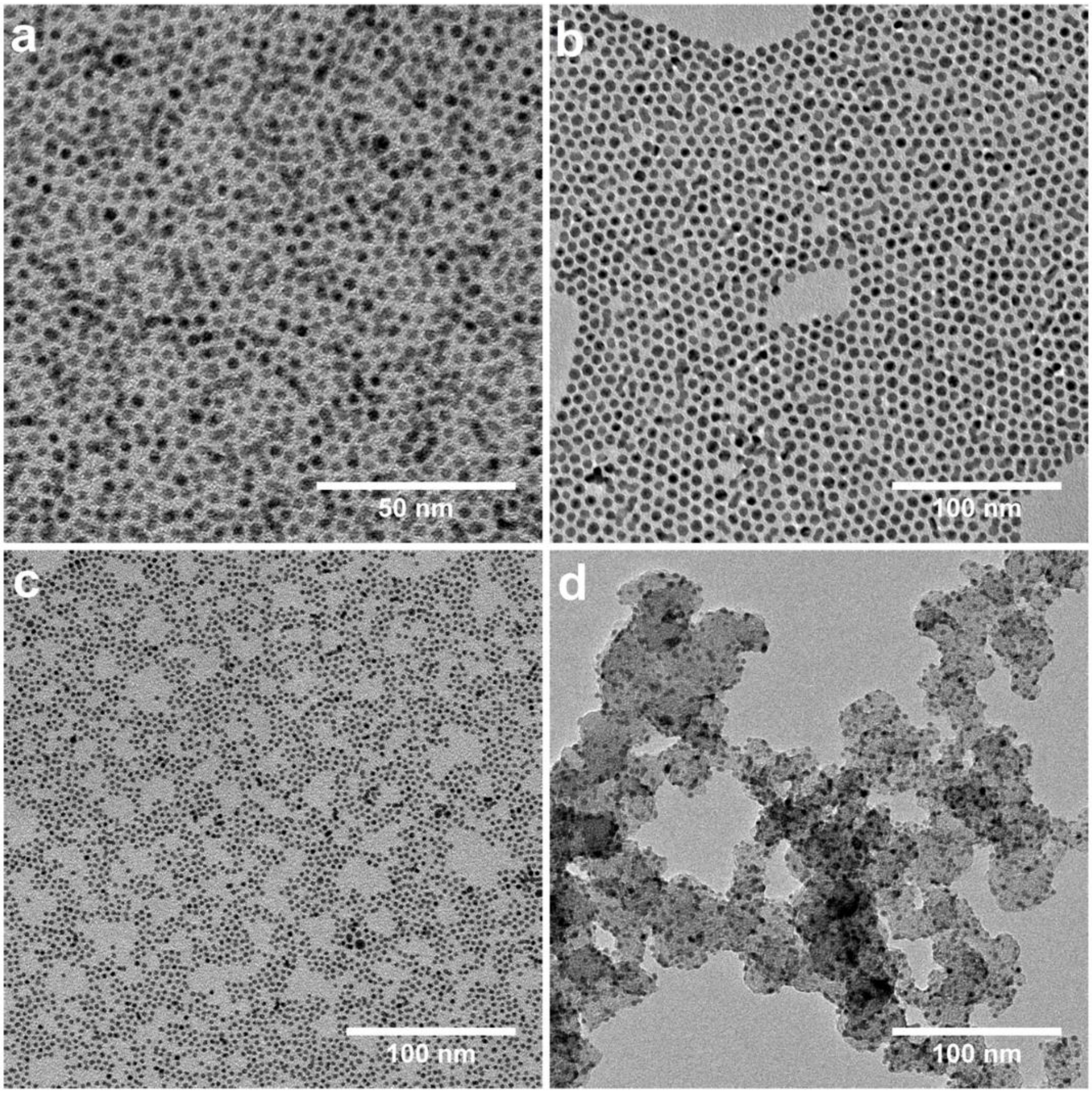

Figure 3.2. TEM images of as-synthesized (a) Ag, (b) Pd, and (c) $Ag_{60}Pd_{40}$ nanoparticles, along with (d) carbon supported $Ag_{60}Pd_{40}$ catalyst after ligand removal.

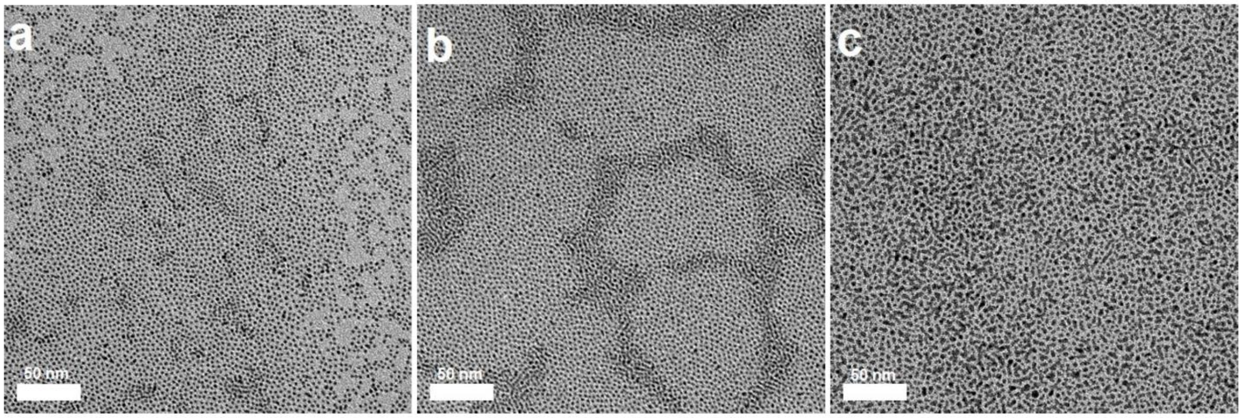

Figure 3.3. TEM images of as-synthesized (a) $Ag_{30}Pd_{70}$, (b) $Ag_{50}Pd_{50}$, and (c) $Ag_{75}Pd_{25}$ nanoparticles.

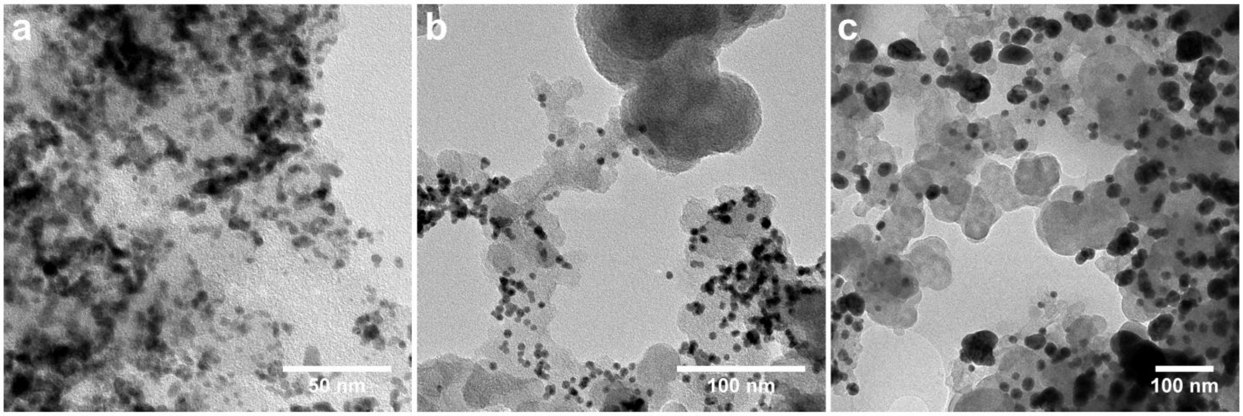

Figure 3.4. TEM images of carbon supported (a) $Ag_{60}Pd_{40}$, (b) Pd, and (c) Ag catalysts after CPE experiments.

CV was employed to create a potential-current profile for the bimetallic and monometallic nanoparticle catalysts, as shown in figure 3.5. Each catalyst displayed an onset of current around 0 V vs. RHE, and the current began to sharply increase for each catalyst around -0.4 V vs. RHE, so we chose to use this as the smallest overpotential in our subsequent CPE studies. Interestingly, the $Ag_{60}Pd_{40}$ nanoparticle catalysts exhibits greater current density before the reductive scan reached -0.5 V vs. RHE compared to the pure Ag or Pd counterparts. This suggests that the AgPd alloy nanoparticles should display better catalytic performance than monometallic catalysts at low overpotentials.

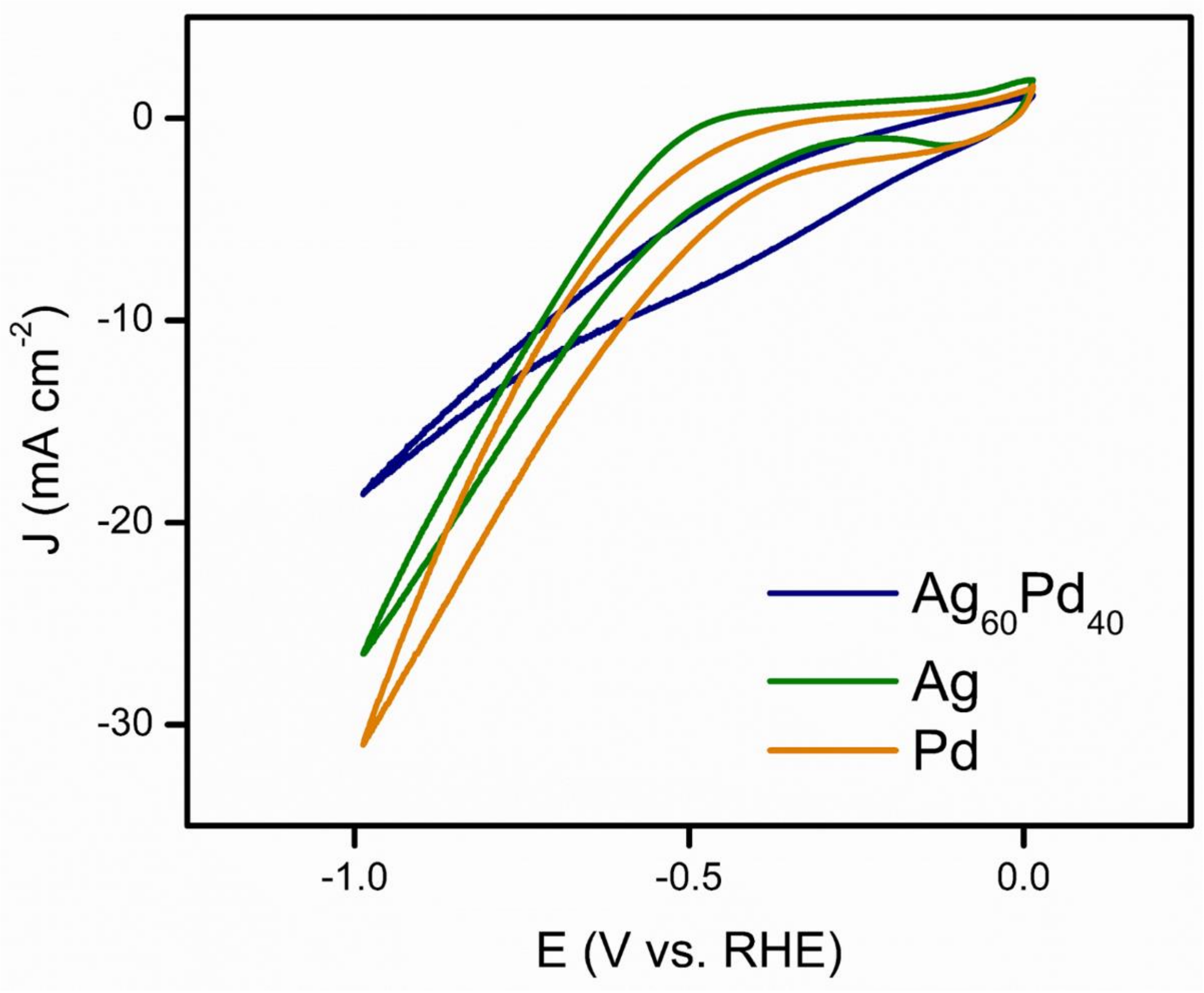

Figure 3.5. CVs of Ag, Pd, and $Ag_{60}Pd_{40}$ nanoparticle catalysts in 0.1 M sodium phosphate buffer solution containing 100 mM furfural.

Each nanoparticle catalyst was tested for furfural electrocatalytic reduction performance by CPE. Figure 3.6 shows the results collected from a typical set of experiments for $Ag_{60}Pd_{40}$, which is highlighted here as an example. Section 3.4 provides detailed equations relevant to our data analysis. Figure 3.6(a) summarizes the furfuryl alcohol yield, carbon balance, and furfural conversion values obtained over six incremental electrolysis experiments from -0.4 V to -0.9 V vs. RHE using $Ag_{60}Pd_{40}$. It shows that both the furfuryl alcohol yield and furfural conversion increase with the use of larger overpotential. Figure 3.6(b) shows the calculated faradaic efficiencies to furfuryl alcohol and H_2 for $Ag_{60}Pd_{40}$ across the range of potentials. Exceptionally high furfuryl alcohol selectivities are obtained at all these overpotentials, where undesired reactions are not occurring to a significant extent. This catalyst produced furfuryl alcohol with greater than 95% faradaic efficiencies at both -0.4 and -0.5 V vs. RHE. Moving towards more negative potentials, a decrease in the faradaic efficiency to furfuryl alcohol was observed. HER

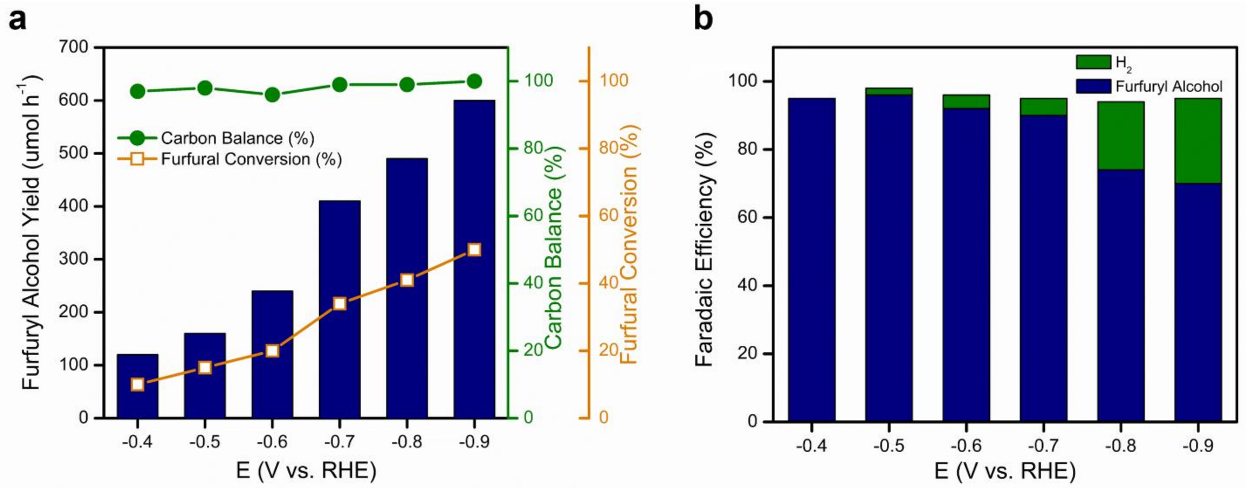

Figure 3.6. Catalytic (a) activity and (b) selectivity results for furfural electrocatalytic reduction using the carbon supported $Ag_{60}Pd_{40}$ catalyst. The furfural conversion is obtained after one-hour CPE at each potential.

began competing with furfural electrocatalytic reduction around -0.6 V for this catalyst, consuming a larger portion of the current at greater applied potentials. It is worth noting that some other side-reactions might participate at higher electrocatalytic reduction overpotentials, but not enough to elicit product identification and quantification in our study.

The catalytic yields and faradaic efficiencies to furfuryl alcohol using different catalysts were compared in figure 3.7, portraying that each bimetallic alloy material performed objectively better than the monometallic Ag and Pd analogues. Using alloy nanoparticles, HER and

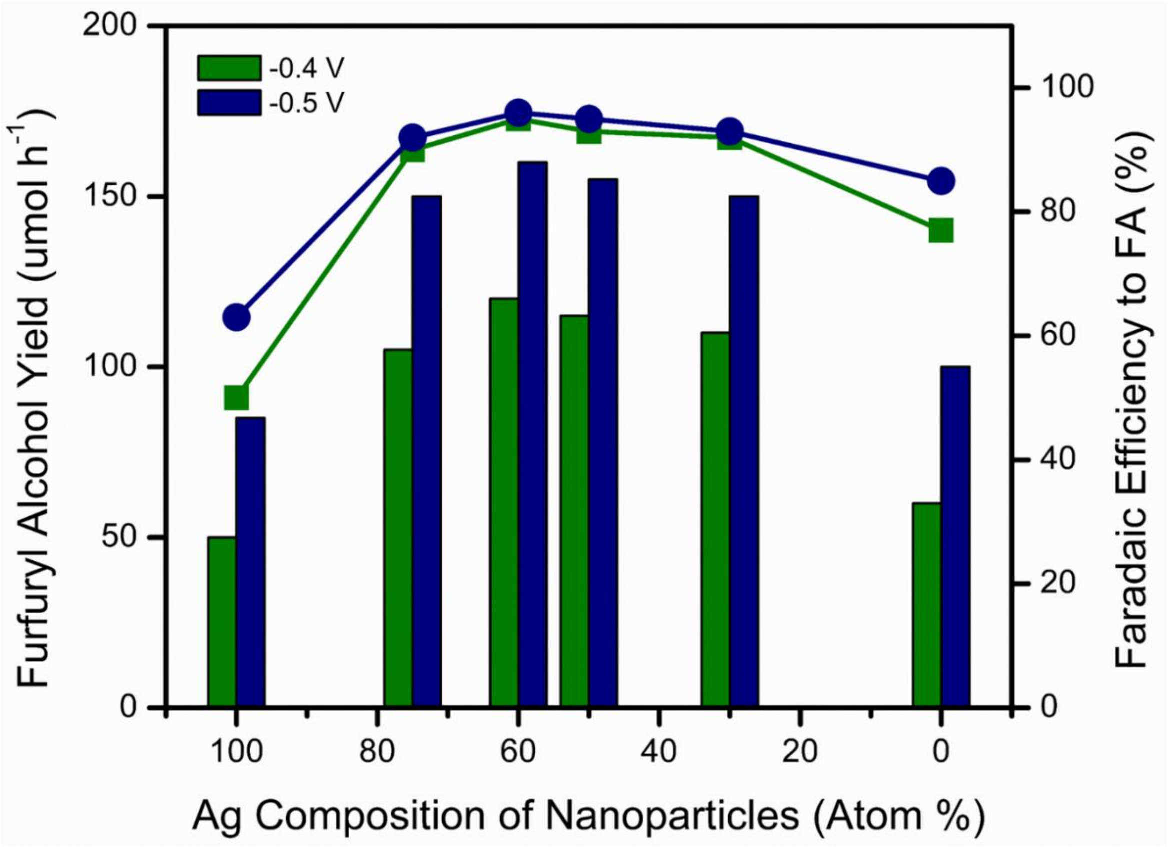

Figure 3.7. Comparison of furfuryl alcohol yields and selectivities measured for nanoparticle catalysts at -0.4 V (green, left bars, squares) and -0.5 V (blue, right bars, circles) vs. RHE.

undesired side reactions occur negligibly in the conditions studied, and exceedingly high current efficiencies towards furfuryl alcohol are observed. The furfuryl alcohol selectivities reported herein for AgPd nanoparticles are outstanding amongst the existing literature.[16] Moreover, plotting the nanoparticle composition against both furfuryl alcohol yield and selectivity reveals a volcano-type trend at low overpotentials, indicating that an alloy with composition $Ag_{60}Pd_{40}$ is the best selection for this electrochemical reaction condition. Our results suggest that for furfural electrocatalytic reduction, metal alloying is an effective strategy to create more efficient nanoparticle catalysts. This is likely ascribed to the aforementioned electronic effects of alloy catalysts, decreasing the affinity of aromatic compounds, and minimizing the poisoning possibility for catalytic sites, as revealed in our previous study of AgPd nanoparticles.[17]

Electrocatalytic reduction of furfural may be conducted in a variety of experimental conditions, selection of which will have significant impacts on chemical process optimization.[18] A recent report has indicated that high selectivities to methylfuran and furfuryl alcohol might be obtained depending on the catalyst and electrocatalytic reduction conditions.[19] In principle, at low pH, the high availability of protons is beneficial to the formation of metal-hydride species which are coupled to both the 4-electron reduction of furfural to methylfuran, and the 2-electron transfer to produce furfuryl alcohol. Low pH raises issues in furfural electrocatalytic reduction when competing HER limits current selectivity to producing the desired furanic product. To compare the furfural electrocatalytic reduction activity of AgPd in different pH conditions, we performed controlled potential electrolysis analyses in different electrolytes using the most active $Ag_{60}Pd_{40}$ catalyst. The catalyst was tested in four different electrolytes for furfural electrocatalytic reduction: 0.1 M H_2SO_4 (pH 0.95), 0.2 M NH_4Cl (pH 4.9), 0.1 M sodium phosphate buffer (pH 6.8), and 0.1 M potassium phosphate buffer (pH 6.9). Figure 3.8 shows pH measurements before and after use in electrocatalytic reduction experiments. Our study has omitted experiments in basic conditions due to a consensus in the literature regarding the instability of furanics at high pH.[19] Reliable electrocatalytic product quantification cannot be performed in basic conditions since non-electrocatalytic processes cause chemical changes in the furanic substrate and products.

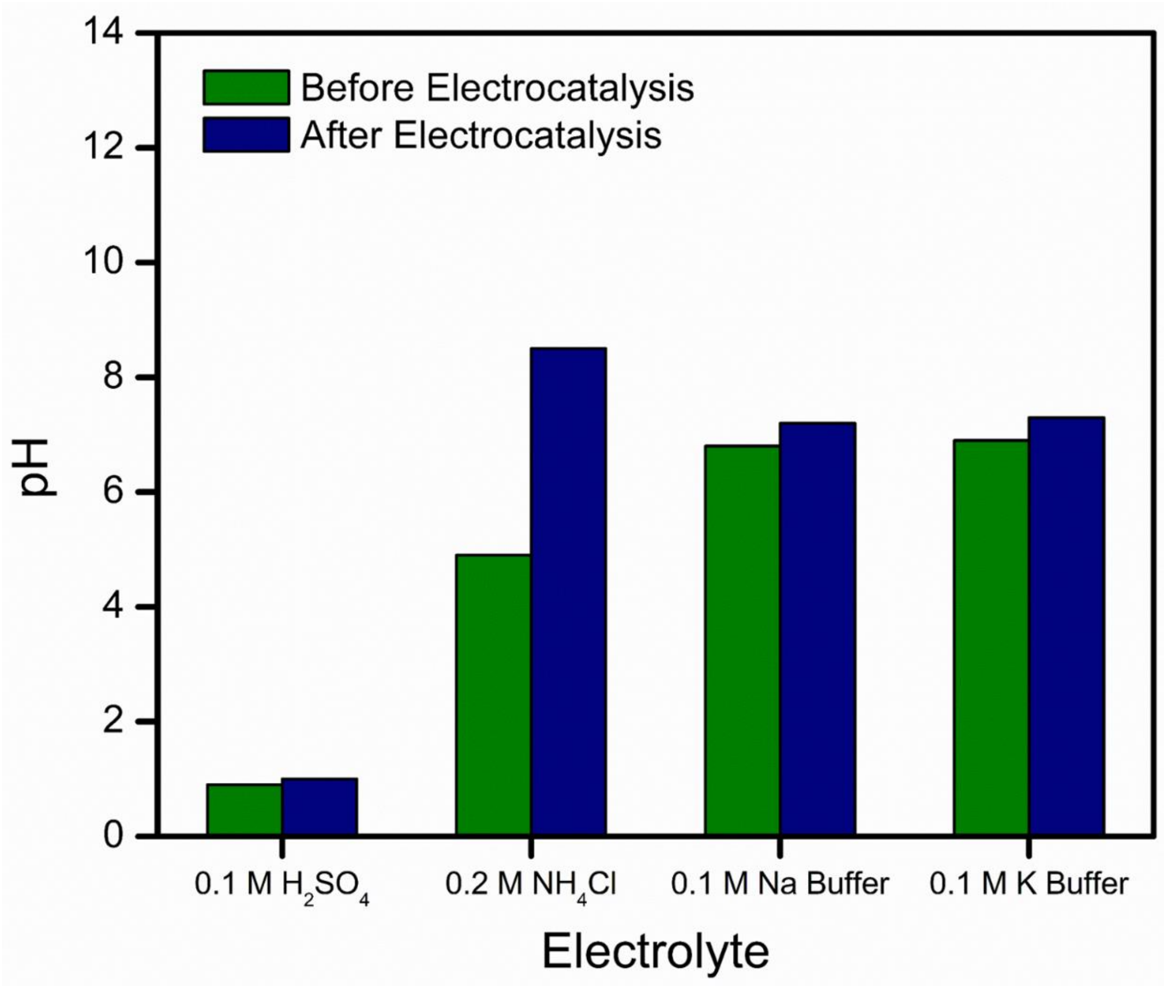

Figure 3.8. Measured pH of different electrolytes before and after CPE tests. CPE was performed using identical working electrodes ($Ag_{60}Pd_{40}$) held at -0.5 V vs. RHE for 1 hour in 12 mL of electrolyte containing 100 mM furfural.

CVs of the $Ag_{60}Pd_{40}$ catalyst in different electrolytes are provided in Figure 3.9. The CV profile for $Ag_{60}Pd_{40}$ in the presence of furfural in neutral buffer electrolyte displays significantly increased reductive current compared with furfural-free condition, suggesting favorable kinetics for furfural to furfuryl alcohol conversion relative to HER in the neutral condition. This claim is supported by results from the CPE tests in neutral buffer at -0.5 V, from which we calculated

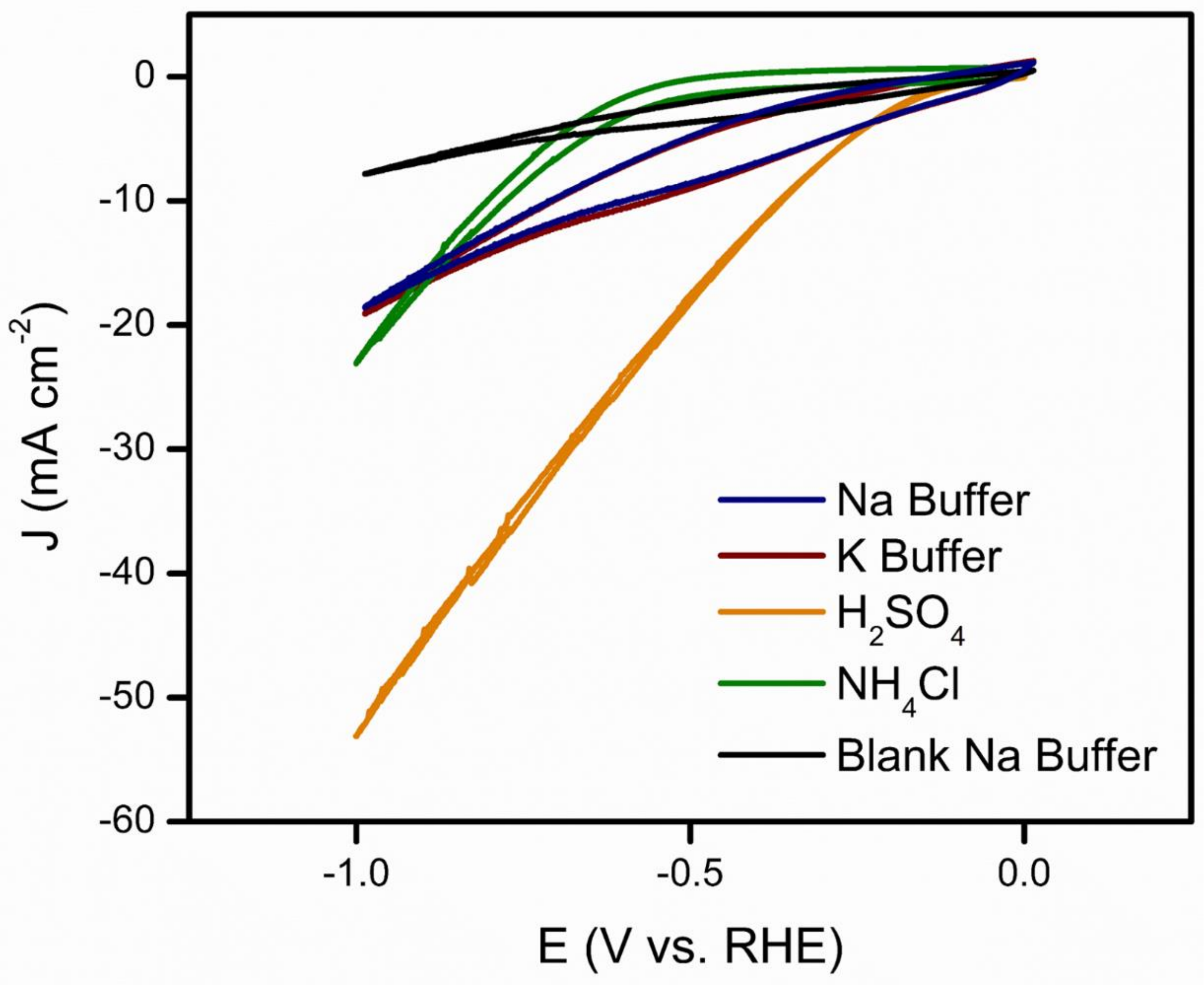

Figure 3.9. CVs of $Ag_{60}Pd_{40}$ catalyst in different aqueous electrolytes containing 100 mM furfural. The experiment labeled “blank Na buffer” did not contain any furfural.

high and low selectivities to furfuryl alcohol and H_2, respectively. Across the range of applied potentials, the measured current density is largest in sulfuric acid electrolyte (pH 0.95), which agrees with other studies detailing the role(s) of protons at the cathode surface during furfural electrocatalytic reduction.[20]

As summarized in Figure 3.10, in comparison to neutral environment, where little H_2 evolution was observed, acidic electrolytes promoted HER with H_2 faradaic efficiencies of 55% and 34% at pH 0.95 and 4.9, respectively, under -0.5 V vs. RHE. Consequently, furfural electrocatalytic

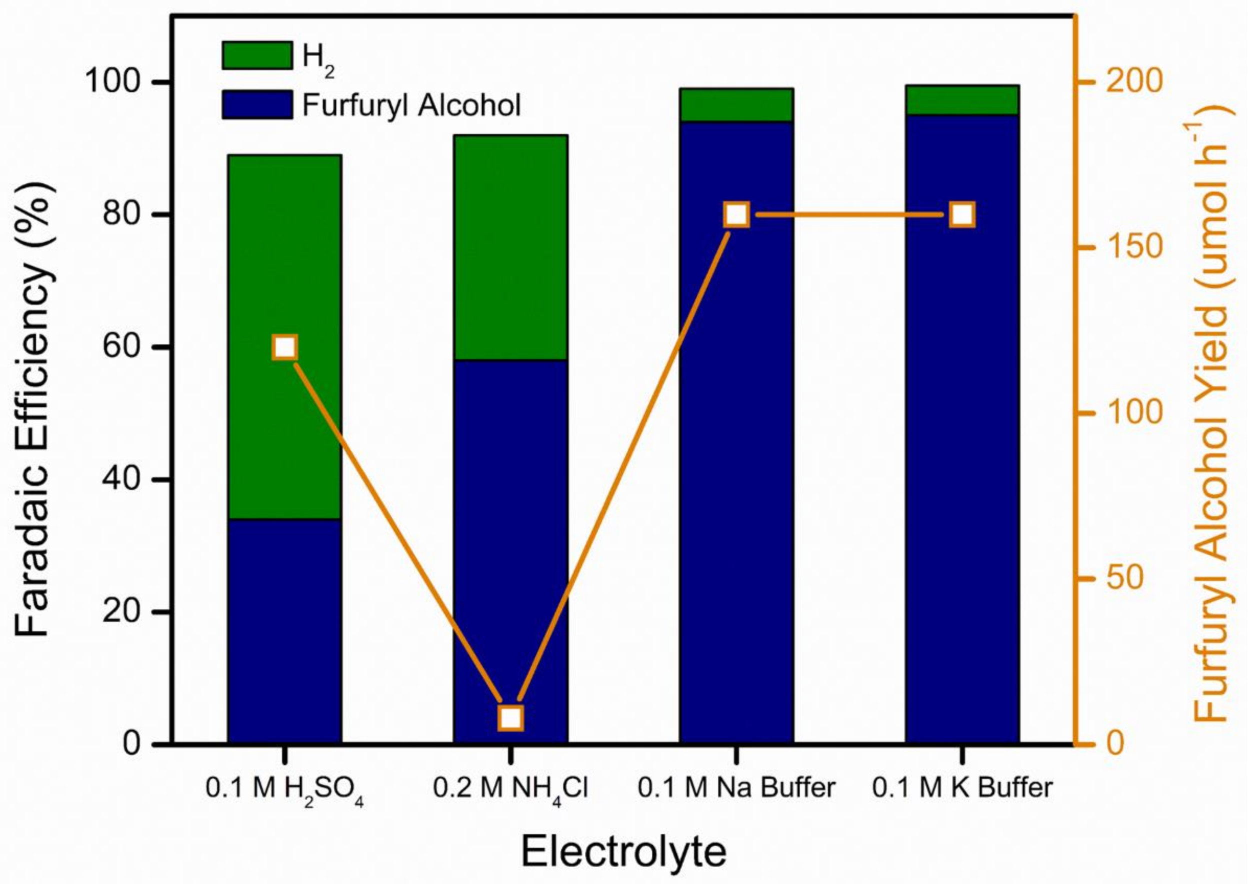

Figure 3.10. Performance comparison of $Ag_{60}Pd_{40}$ catalyst for furfural electrocatalytic reduction in different electrolyte conditions. The CPE tests were performed at -0.5 V vs. RHE.

reduction selectivities to furfuryl alcohol are unimpressive in acidic conditions. Figure 3.11 shows that the furfural conversion through one-hour CPE in 0.1 M H_2SO_4 exceeds that of the neutral systems, which can be attributed to higher proton concentration and larger coverage of adsorbed hydride (H*), since mechanistic investigations of electrocatalytic reduction generally implicate H* as reactant in reductive electrocatalytic synthesis.[14] Carbon balances were measured well below 100% in acidic electrolytes, indicating the formation of some other furanic

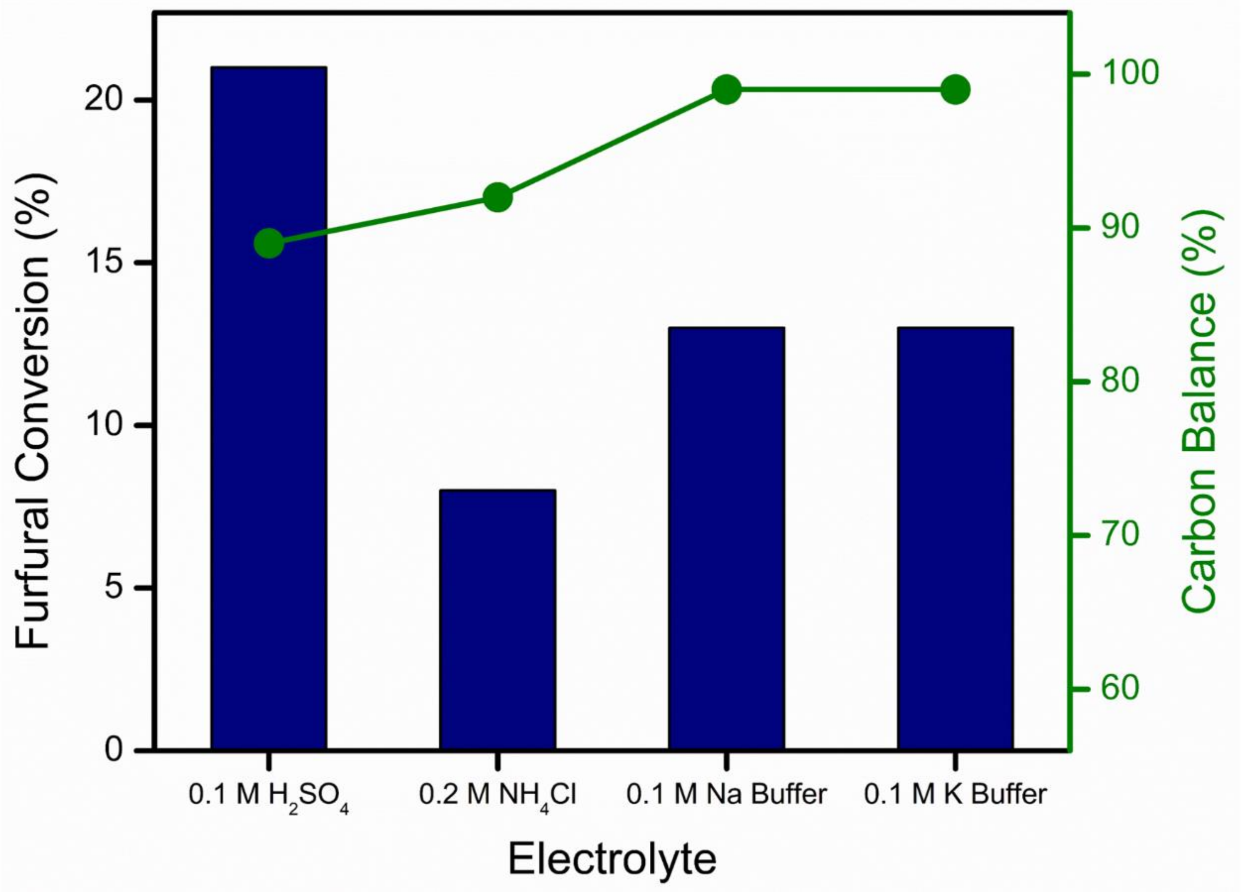

Figure 3.11. Catalytic activity results of $Ag_{60}Pd_{40}$ catalyst for the electrocatalytic reduction of furfural in different electrolytes. CPE was performed using identical working electrodes held at -0.5 V vs. RHE for 1 hour in 12 mL of electrolyte containing 100 mM furfural.

species like methylfuran, hydrofuroin, or polymeric resins, which were not quantified in the scope of this report. In NH_4Cl, furfuryl alcohol yield was far below that of the other electrolytes tested, as was the measured current density at -0.5 V vs. RHE, but it is worth noting that a large increase in pH was observed after performing bulk electrolysis in the 0.2 M NH_4Cl electrolyte, whereas the other electrolytes did not undergo any significant pH change (Figure 3.8). In addition, we find there were virtually no differences in the furfural electrocatalytic reduction results using phosphate buffer with different cations (Na^+ or K^+). We conclude that neutral environment enables a balance between furfuryl alcohol production and HER suppression, according to respectively high and low FEs.

3.3 Summary

In summary, we studied the bimetallic alloy composition effect on furfural electrocatalytic reduction performance. $Ag_{60}Pd_{40}$ nanoparticles were identified with the highest catalytic activity and selectivity for furfuryl alcohol production, superior to Ag and Pd monometallic counterparts and other AgPd nanoparticles. The neutral buffer electrolyte was found to be the most suitable reaction condition for efficient furfuryl alcohol production due to low furfural reduction overpotentials, along with suppression of HER or other competing processes at neutral pH. This work highlights the crucial role and encouraging potential of alloy nanoparticle catalysts in electrochemical upgrading of biomass-derived platform chemicals.

3.4 Experimental

Chemicals and Materials

All reagents were used without further purification. Silver acetate (Ag(Ac), 99%), oleylamine (70%), oleic acid (90%), and Nafion (5 wt%) perfluorinated resin solution were purchased from Sigma-Aldrich. Palladium acetylacetonate ($Pd(acac)_2$, 35% Pd) and 1-octadecene (90%) were purchased from Acros Organics. 2-propanol (>99.5%), hexane (>98.5%) and acetonitrile (HPLC grade) were purchased from Fisher Chemical. Ethanol (200 proof) was purchased from Decon Labs. Ammonium chloride (NH_4Cl) was purchased from VWR Chemicals, and sulfuric acid solution (H_2SO_4, 50 wt% in water) was purchased from Honeywell. Vulcan carbon (XC-72R), carbon paper (Toray paper 060), and the Nafion membrane (Nafion 212) used in our electrochemical cell were purchased from Fuel Cell Store.

Synthesis of AgPd Nanoparticles

We synthesized AgPd nanoparticles using a previously reported method which produces nanoparticles with different alloy compositions.[15] In a typical synthesis of $Ag_{60}Pd_{40}$ nanoparticles, 0.10 g of Ag(Ac) (0.6 mmol) and 0.12 g of $Pd(acac)_2$ (0.4 mmol) were dissolved in 0.5 mL of oleic acid, 4.5 mL of oleylamine, and 10 mL of 1-octadecene. The solution was kept under vacuum to remove the moisture, and then held under gentle N_2 flow for the entire reaction. Using a temperature-controlled heating mantle, the system was heated to 60 °C, held until a homogenous solution formed, and then the temperature was increased to 180 °C at about 4 °C / min. At 150 °C, the color of the solution changed from transparent yellow to opaque dark-brown, and the reaction was held at 180 °C for 20 minutes to ensure sufficient nanoparticle ripening. The solution was cooled to room temperature and the nanoparticles were collected by precipitation using 50 mL of 2-propanol and centrifugation at 9500 rpm for 8 minutes. The precipitated nanoparticles were then re-dispersed in hexane, washed with 40 mL of ethanol, and separated by another centrifugation (9500 rpm, 8 min). The nanoparticles were finally stored in hexane for later use. With the total moles of metal precursor held constant at 1 mmol metal, the masses of Ag(Ac) and $Pd(acac)_2$ were varied between experiments to make nanoparticles with different relative atomic compositions of Ag and Pd. For example, to prepare a sample of

$Ag_{50}Pd_{50}$ nanoparticles, the synthesis would include 0.5 mmol of Ag(Ac), and 0.5 mmol of $Pd(acac)_2$. The atomic ratio of Ag/Pd in the resultant AgPd nanoparticles is consistent with the molar ratio of $Ag(Ac)/Pd(acac)_2$. The atomic ratio of Ag and Pd in each nanoparticle sample was determined using inductively coupled plasma – optical emission spectroscopy (ICP-OES).

Preparation of Carbon Supported Nanoparticle Catalysts

The nanoparticles were deposited onto conductive carbon support to prepare the electrocatalyst. Vulcan carbon was first dispersed in hexane by sonication for 20 minutes, and then metal nanoparticles, also in hexane, were added to the mixture under sonication for 1 hour. The mass composition for each catalyst material was 40% of Vulcan carbon and 60% of metal. The carbon supported nanoparticle catalyst was collected by centrifugation (8500 rpm, 8 min), and then washed with ethanol twice. To remove bulky organic ligands from the metal nanoparticle surfaces, the catalyst was stirred in 40 mL of acetic acid at 70 °C overnight under N_2 atmosphere. After this, the mixture was washed with 40 mL of ethanol and separated by centrifugation (8500 rpm, 8 min), and then the catalyst was washed twice more. Lastly, the catalyst was dried overnight under vacuum. The metal mass loading amount for carbon supported catalysts was confirmed by inductively coupled plasma – optical emission spectroscopy (ICP-OES).

Fabrication of Working Electrodes

The catalyst, in the form of an ink, was air-brushed onto carbon paper to develop the working electrodes for our electrochemical tests. To make the ink, a measured amount of dried catalyst plus 10 wt% of Nafion were sonicated for one hour in ethanol. The homogenous dispersion was sprayed through an airbrush onto both sides of carbon paper (1 cm^2). The carbon paper was left to dry in ambient condition and used as the working electrode. The metal loading on carbon paper was kept at 0.6 $mg_{metal}\ cm^{-2}$ for all catalysts.

Electrocatalytic Measurements and Analysis

All electrochemical experiments were performed in an H-type cell with two compartments separated by a Nafion 212 membrane. Each chamber contained 12 mL of aqueous electrolyte composed of 100 mM furfural. A stir plate was used at 700 rpm in the cathodic chamber, and there was no stirring for the anolyte. The counter electrode was Pt mesh in the anodic chamber. The cathodic chamber was sealed with a customized rubber cap which used Teflon capillary tubes to bubble N_2 gas into the catholyte and to collect gas from the cathodic chamber headspace, feeding it directly into a gas chromatographer. An external calibration curve was used to quantify the concentration of H_2 in the cathodic gas stream during constant potential electrolysis (CPE) experiments. The catholyte was purged of air under simultaneous stirring and N_2 bubbling at 100 sccm for 20 minutes before every experiment, and then the N_2 flow was lowered to 10 sccm for the duration of the experiment. The working electrode and the Ag/AgCl reference electrode were placed in the cathodic chamber.

The electrochemical study was conducted using an Autolab PGSTAT302N potentiostat. At the start of each experiment, a CV tested the quality of the working electrode and the setup to ensure repeatability of the potential / current profile. A representative CV is displayed in Figure S3 for both pure nanoparticle catalysts and $Ag_{60}Pd_{40}$. Stirring was stopped to perform each CV experiment, then restarted before conducting the subsequent CPE experiment. CPE was performed at a desired potential for one hour, after which the catholyte was collected for product analysis. The electrolyte in both chambers was refreshed before each set of experiments. High-pressure liquid chromatography (HPLC, Shimadzu) was used for liquid product analysis.

The relevant equations for the calculations in this report are listed below. *F* is Faraday's constant. *C* is the amount of charge passed in Coulombs over the course of 1-hour CPE experiments. *n* is the number of electrons passed for each reduction reaction: it is equal to two for both HER and furfural to furfuryl alcohol conversion. $[\text{Furfural}]_{\text{initial}}$ is the concentration of furfural calculated from HPLC analysis of each furfural-containing electrolyte without electrocatalytic testing. $[\text{Furfural}]_{\text{post-CPE}}$ and $[\text{furfuryl alcohol}]_{\text{post-CPE}}$ were determined from HPLC analysis of the catholyte after use in CPE experiments. The moles of furfuryl alcohol were calculated by multiplying $[\text{furfuryl alcohol}]_{\text{post-CPE}}$ by the volume of the catholyte (12 mL).

$$Faradaic\ Efficiency_{furfuryl\ alcohol} = \frac{moles_{furfuryl\ alcohol} nF}{C} * 100\%$$

$$Faradaic\ Efficiency_{H_2} = \frac{moles_{H_2} nF}{C} * 100\%$$

$$Furfural\ Conversion = \frac{[furfural]_{initial} - [furfural]_{post-CPE}}{[furfural]_{initial}} * 100\%$$

$$Carbon\ Balance = \frac{[furfuryl\ alcohol]_{post-CPE} + [furfural]_{post-CPE}}{[furfural]_{initial}} * 100\%$$

Other Physical Characterizations

TEM images were obtained on a Tecnai Spirit at 120 kV equipped with a tungsten filament. Compositional characterizations of our catalysts were conducted by ICP-OES using a Perkin

Elmer Avio 200. All electrolytes were prepared using Ultrapure (Type I) water dispensed through a Millipore Synergy purification system, and pH measurements were made using a Mettler Toledo FiveEasy pH meter. Liquid products were analyzed on a Shimadzu HPLC equipped with two LC-20AD pumps, using a Phenomenex Luna Omega C18 column for separation. The aqueous mobile phase contained 15% acetonitrile with a gradient flow method in which the acetonitrile concentration is gradually increased to 60%, and then lowered back to 15%. A diode array detector (Shimadzu SPD-M20A) and external calibration curves were used to determine the concentration of furfural and furfuryl alcohol. H_2 was quantified by feeding the cathodic headspace directly into a Shimadzu GC-2014 gas chromatographer equipped with both thermal conductivity detector (TCD) and flame ionization detector (FID).

3.5 References

1 Tuck, C. O., Pérez, E., Horváth, I. T., Sheldon, R. A., Poliakoff, M., *Science*, **2012**, *337*, 695-699.

2 Hill, J., Nelson, E., Tilman, D., Polasky, S., Tiffany, D., *Proceedings of the National Academy of Sciences*, **2006**, *103*, 11206-11210.

3 Kwon, Y., Schouten, K. J. P., van der Waal, J. C., de Jong, E., Koper, M. T. M., *ACS Catalysis*, **2016**, *6*, 6704-6717.

4 Long, J., Xu, Y., Zhao, W., Li, H., Yang, S., *Frontiers in Chemistry*, **2019**, *7*.

5 Dumeignil, F., Capron, M., Katryniok, B., Wojcieszak, R., Löfberg, A., Girardon, J. S., Paul, S., *Journal of the Japan Petroleum Institute*, **2015**, *58*, 257-273.

6 Chadderdon, X. H., Chadderdon, D. J., Matthiesen, J. E., Qiu, Y., Carraher, J. M., Tessonnier, J. P., Li, W., *Journal of the American Chemical Society*, **2017**, *139*, 14120-14128.

7 Green, S. K., Lee, J., Kim, H. J., Tompsett, G. A., Kim, W. B., Huber, G. W., *Green Chemistry*, **2013**, *15*, 1869-1879.

8 Mariscal, R., Maireles-Torres, P., Ojeda, M., Sádaba, I., López Granados, M., *Energy & Environmental Science*, **2016**, *9*, 1144-1189.

9 Jung, S. & Biddinger, E. J., *ACS Sustainable Chemistry & Engineering*, **2016**, *4*, 6500-6508.

10 Peng, Y., Cui, M., Zhang, Z., Shu, S., Shi, X., Brosnahan, J. T., Liu, C., Zhang, Y., Godbold, P., Zhang, X., Dong, F., Jiang, G., Zhang, S., *ACS Catalysis*, **2019**, *9*, 10803-10811.

11 Chamoulaud, G., Floner, D., Moinet, C., Lamy, C., Belgsir, E. M., *Electrochimica Acta*, **2001**, *46*, 2757-2760.

12 Cao, Y. & Noel, T., *Organic Process Research & Development*, **2019**, *23*, 403-408.

13 Nilges, P. & Shroeder, U., *Energy & Environmental Science*, **2013**, *6*, 2925-2931.

14 Lopez-Ruiz, J. A., Andrews, E., Akhade, S. A., Lee, M., Koh, K., Sanyal, U., Yuk, S. F., Karkamkar, A. J., Derewinski, M. A., Holladay, J., Glezakou, V., Rousseau, R., Gutiérrez, O. Y., Holladay, J. D., *ACS Catalysis*, **2019**, *9*, 9964-9972.

15 Zhang, S., Metin, O., Su, D., Sun, S. H., *Angewandte Chemie International Edition*, **2013**, *52*, 3681-3684.

16 Kim, S., Kwon, E. E., Kim, Y. T., Jung, S., Kim, H. J., Huber, G. W., Lee, J., *Green Chemistry*, **2019**, *21*, 3715-3743.

17 Cui, M., Johnson, G., Zhang, Z., Li, S., Hwang, S., Zhang, X., Zhang, S., *Nanoscale*, **2020**, *12*, 14068-14075.

18 Jung, S. & Biddinger, E. J., *Energy Technology*, **2018**, *6*, 1370-1379.

19 May, A. S. & Biddinger, E. J., *ACS Catalysis*, **2020**, *10*, 3212-3221.

20 Jung, S., Karaiskakis, A. N., Biddinger, E. J., *Catalysis Today*, **2019**, *323*, 26-34.